Rock–Water Interaction Group

Institute of Geological Sciences,

University of Bern

Baltzerstrasse 1–3, 3012 Bern, Switzerland

Assessing geochemical issues expected during High Temperature Aquifer Thermal Energy Storage (HT-ATES) in the Mesozoic limestones of the Geneva Basin

October, 2021

Authors:

Dr. Daniela B. van den Heuvel, Dr. Christoph Wanner, Joshua P. Richards,
Prof. Larryn W. Diamond

Table of Contents

Outline

As part of the Geothermica Heatstore project, the Geneva basin is under investigation for potential high temperature aquifer thermal energy storage. This report presents an assessment of the different topics that were tackled by our team at the Institute of Geological Sciences, University of Bern:

- Part 1: Experimental assessment of mineral reactions in a potential reservoir formation (Kimmeridgian carbonates) as well as mineral scaling in the surface installations during HT-ATES.
- Part 2: Corrosion and scaling during by geochemical and/or microbial processes during a shut-in of the GEo-01 well.
- Part 3: Implications for a potential HT-ATES system in the Mesozoic limestones of the Geneva Basin.

For a review of other problems which could be of relevance for a planned HT-ATES system in the Geneva Basin, as they have been encountered in previous HT-ATES projects, see our literature compilation in the report on the Geospeicher Forsthaus (van den Heuvel et al., 2021).

1. Mineral reactions inside the reservoir

1.1. Background

When hot water is injected into an aquifer, it will interact with the minerals present. The most important reactions in an HT-ATES reservoir are mineral dissolution and precipitation as they change the fluid composition and can lead to an (undesired) redistribution of porosity and fluid flow pathways inside the reservoir. In the carbonate reservoirs of the Geneva basin, the following reactions are most likely to occur:

(1) Dissolution/precipitation of carbonates

(2) Dissolution of silicate minerals

Generally, formation water is used as the working fluid in the operation of a HT-ATES site. The water is therefore saturated with respect to the minerals present in the reservoir under *in-situ* physico-chemical conditions. Upon extraction from the formation and heating in the heat exchanger, the water becomes undersaturated with respect to minerals with a normal (prograde) solubility, such as most silicates. Thus, upon reinjection, the hot water is capable of dissolving any silicate minerals in the reservoir until saturation with respect to that mineral is reached. Mineral such as carbonates, on the other hand, become supersaturated during heating due to their retrograde solubility. Depending on the precipitation rates of the carbonate minerals and on the injection rates, the fluid can either be injected in a supersaturated or saturated state. If precipitation rates are low and no/little precipitation takes

place in the surface installations, the fluid is still supersaturated upon entering the reservoir, and carbonates might precipitate close to the wells until the fluid is saturated with respect to these minerals. If precipitation in the surface installations is rapid (= mineral scaling), the fluid is already saturated when injected. In either case, carbonates may dissolve at some distance away from the borehole as the water cools when moving further into the reservoir, becoming undersaturated again.

In order to evaluate which of these possible mineral reactions are likely to occur in the target reservoir of the Geneva heat storage system, we conducted so called "batch experiments". In these experiments, we mix rock fragments with an artificial pore water (APW) and heat them to different temperatures. Fluid samples are taken at different time intervals in order to evaluate the changing fluid composition as a function of time. By attempting to replicate the observed trends using different mineral reactions in a kinetic model, reactions (un)likely to occur can subsequently be identified.

1.2.   Materials & Methods

1.2.1. Batch experiments

The batch experiments were designed to replicate the rock-water interaction occurring in the target reservoir during heat storage. This replication was done by mixing rock fragments representative of the potential reservoir (Kimmeridgian carbonates; Section 1.2.2.) with an artificial porewater based on groundwater in the region (Section 1.2.3.). The two components were allowed to react over 13 days at three different temperatures. The vessels were sampled at specific time intervals throughout the experiment allowing changes in fluid composition to be monitored as a function of time. The mineral reactions taking place were identified by comparing the composition of the solution before and after the experiments.

Batch experiments were performed in 50 cm^3 titanium reactor vessels (Figure 1), originally constructed for the hydrothermal experiments reported by Chermak and Rimstidt (1990). In order to sample fluids without opening the vessels, new lids containing two sampling ports were designed and fabricated. PEEK capillaries and micrometering valves were installed. Care was taken to ensure the capillaries did not reach the bottom of the vessel; this would limit swirling up of the rock fragments during sampling. Before filling the vessels, all parts were cleaned with 5 vol. % HNO3 and subsequently rinsed with ultrapure water and ethanol and dried at 110 °C.

The APW and rock components (see below) were combined inside the 50 cm^3 titanium vessels in quantities of 45 ml and 5 g, respectively. Once the containers were filled, they were closed and tightly sealed. A clamp was attached to the outside of the vessels, and they were mounted onto a rotisserie unit (~ 10 rpm) inside an oven set to the desired experimental temperature. The first set of vessels was left to react at 90 °C experiment, followed by a subsequent experiment at 60 °C and one at room temperature (ca. 20 °C), which was run

simultaneously with the 90 °C runs outside the oven. Instead of titanium vessels, 50 mL centrifuge tubes were filled with rock fragments and APW for the room temperature experiment. They were then placed into an end-over-end shaker at roughly 10 rpm. Sampling was done by simply opening the centrifuge tubes and extracting the fluid using a syringe.

Each experiment was run for 13 days. Vessels were sampled in duplicates at each time points within that period; 0, 0.25, 0.5, 1, 3, 7 and 13 days. The 60 °C experiments were conducted last. Due to this, several fittings had suffered damage from general wear and tear, and had to be replaced. However, supply was limited due to Covid-19 and only 6 out of 12 vessels could be refitted. The experiments, therefore, had to be carried out in two parts: the first set sampling three time steps between 0.25 and 1 days and then another set sampling between 3 and 13 days. For each of the two parts, a new batch of APW was mixed. Due to this, slight variations in the initial conditions of the experiments at 60 °C are present.
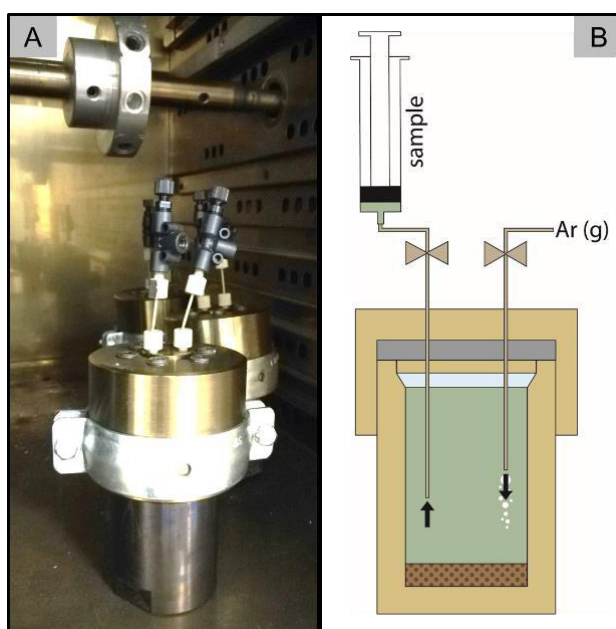

Figure 1. Experimental set-up of batch experiments: Ti-vessel with holder inside rotisserie oven (A). One of the disks to which the samples are attached can be seen in the background above the vessels. The inside of the vessels and the sampling set-up (Ar on one side and syringe on the other) is shown schematically (B). The same conditions are established in all vessels, and they are opened at different times to establish a time series.

At the end of the experiment, the samples were detached from the rotisserie unit and removed from the oven immediately before sampling, which allowed the sampling of the solutions as close to the reaction temperature as possible. Sampling of each vessel took in the order of 10 minutes, and it is assumed that, due to the thick-walled design of the vessels, the temperature of the solution did not drop substantially during sampling. To facilitate fluid sampling, an Ar pressure line (~ 2 bar) was attached to one of the valves, while a syringe was

attached to the second valve. The Ar pressure allowed for easy sampling of solutions without the ingress of any air (Figure 1B). Potentially present suspended solids were removed for all samples by filtering through 0.2 µm syringe filters immediately after sampling. Different aliquots (~ 20 mL) were taken: one, non-acidified for analysis of anions, alkalinity and TIC/TOC, and another one acidified to pH ~ 2 for analysis of cations by adding 1-2 drops of concentrated HNO_3. For all non-acidified samples, the pH was measured immediately after sampling. The samples were analysed for pH, alkalinity and TIC/TOC on the same day, while analyses of anions and cations were performed up to 4 weeks later. In the meantime, samples were stored at 5 °C.

1.2.2. Characterisation of rock material

Rock material mimicking the Kimmerdigian reservoir rocks was obtained from a well drilled at a quarry south of Plagne (Dept. Ain, France). The rocks are part of the Kimmeridgian Formation des Etiollets. Four samples were taken (Figure 2), two each from the Complexe Récifal and the underlying Calcaires de Tabalcon. A section of each core was broken using a hammer, and the fragments were crushed in a jaw crusher. The size fraction 0.35 < x < 0.70 mm was then separated, rinsed with DI water to remove any fines formed during crushing and dried at 40 °C for a few days in preparation for the batch experiments. Some of the size fraction < 0.35 mm was additionally milled to create a fine powder for compositional analyses.

The mineralogical composition of the samples was quantified using X-ray diffraction (XRD) by mixing a powdered aliquot with 20 wt.% corundum powder (internal standard) in a McCrone XRD mill. Two aliquots (a and b) were prepared. Both were analysed using a PANalytical CubiX3 diffractometer (CuKα1; 5-60° 2θ; 0.02°/step), and quantification was done by Rietveld refinement using the PANalytical software High-Score Plus with an analytical uncertainty of about 5 wt.%.

For the analysis of total carbon, nitrogen and sulphur (CNS), 30 mg of fine rock powder was weighed into a small tin capsule. The samples were then analysed on a Thermo Fisher Elemental Analyzer FlashSmart NCS. Detection limits are 0.02 wt.% for TC, 0.01 wt.% for TN and 0.02 wt.% for TS. In order to also determine the contents of total inorganic carbon TIC and total organic carbon TOC of the sample, additional aliquots are weighed in. These aliquots are placed in silver capsules, 1 M HCl is added and left to react at 50 °C for 15 h. This completely removes inorganic carbon from the sample. The leached aliquot is then dried and analysed using the same approach as described above, yielding the TOC content of the material.

In addition, three 4 x 2.5 x 1 cm blocks were cut to prepare polished, not covered thin sections (~ 25 µm thick). For each thin section, one half was dyed using the following solutions:

- Solution A: 1 g potassium hexacyanidoferrat III is dissolved in 100 mL of 1 vol.% HCl

- Solution B: 0.1 g Alizarin is dissolved in 100 mL of 1 vol.% HCl

Solutions A and B are then mixed with a ratio of 2:3 to produce solution C. The thin sections are dipped into solution 2 for one minute, then into solution 3 for 10 seconds and rinsing with ultrapure water. The dyed samples are then air-dried. This process stains the different carbonate minerals depending on their structure and Fe-content: calcite - red, Fe-calcite - purple, dolomite - colourless, Fe-dolomite (ankerite) - blue/green (Dickson, 1966). Therefore, the different carbonate minerals can be distinguished using a petrographic microscope. Observations were made by transmitted light microscopy (Olympus BX51 polarising microscope) equipped with an Olympus UC90 digital camera (software Stream Essential).

1.2.3. Preparation of artificial pore water

Besides the rock material, an artificial pore water (APW) is needed for the batch experiments. The composition of the APW was based on the composition of a groundwater sampled from the Calcaires de Tabalcon in the GEo-2 borehole (Table 1). The APW was prepared according to the instructions in Wersin et al. (2013) and the following chemicals were used (all Merck, ACS reagent grade):

- Sodium bicarbonate ($NaHCO_3$, M = 84.01 g/mol)
- Calcium chloride dihydrate ($CaCl_2 \cdot 2H_2O$, M = 147.01 g/mol)
- Potassium chloride (KCl, M = 74.55 g/mol)
- Magnesium sulfate heptahydrate ($MgSO_4 \cdot 7H_2O$, M = 246.51 g/mol)
- Magnesium chloride hexahydrate ($MgCl_2 \cdot 6H_2O$, M = 203.31 g/mol).

To prevent the formation of metastable salts that are difficult to dissolve, three separate initial solutions were prepared:

(1) The Na- and K-salts were dissolved in 1/2 of the final volume of ultrapure water (Solution 1).

(2) The Mg-salts were dissolved in 1/4 of the final volume of ultrapure water (Solution 2).

(3) The Ca-salts were dissolved in 1/4 of the final volume of ultrapure water (Solution 3).

Solution 1 and 2 mixed and shaken well before solution 3 was added. As several cations have to be added as soluble chloride salts, the Cl concentration in the APW is higher than in the in-situ groundwater. However, chloride is a passive species not involved in any expected dissolution or precipitation reaction. Thus, the excess chloride is not expected to significantly affect the outcome of the experiments.

Table 1. Chemical composition of a groundwater sampled in the Calcaires du Tabalcon formation (GEo-02) in July 2020. Data provided by University of Geneva.

Geo-2 Borehole	
pH	8.22
Log pCO_2 (at cc sat)	-1.95
	mg/L
Ca	35
Mg	14.2
K	5.35
Na	52.5
Cl	15
SO_4	32.1
Alkalinity	179

The APW was mixed under atmospheric pressure conditions ($pCO_2 = 10-3.5$ bar) for practical reasons. The solution was then bubbled with N_2 for 30 min while stirring to remove the dissolved oxygen. In a second step, the solution was bubbled for another 30 min with a CO_2/Ar mixture ($pCO_2 = 10^{-2.2}$ bar) to establish a higher pCO_2 for the experiments. Unfortunately, the thus established pCO_2 is lower than the reconstructed value in the reservoir (Table 1). However, no gas mix with a higher pCO_2 was available to run the experiments. Once prepared, an aliquot of the finished solution was taken and analysed for each batch of APW prepared.

1.2.4. Solution analyses

Main cation and anions were analysed by ion chromatography (IC) using a Metrohm 850 Professional IC and the MagIC Net 3.3 (2019) software. The IC is equipped with a Metrosep C4-150/4.0 separation column for cation analyses, combined with a Metrosep C4 Guard/4.0 pre-column and an upstream Metrosep RP 2 Guard/3.5 column. The eluent is composed of a 1.7 mM HNO_3- and 0.7 mM dipicolinic acid solution. The IC is equipped with a Metrosep ASupp7-250/4.0 column for anion analyses, combined with a Metrosep ASupp 4/5 Guard/4.0 pre-column and an upstream Metrosep RP 2 Guard/3.5 column (Nr. 6.1011.030). The eluent is composed of 3.6 mM Na_2CO_3. For the preparation of the eluent solutions, ultrapure reagents from commercial producers were used. Certified calibration and check standards were obtained from the same suppliers. For cations, the quantification limit is 0.1 mg/L with an analytical error of $\pm$ 6 % for Na, $\pm$ 9 % for K, $\pm$ 4 % for Mg and $\pm$ 8 % for Ca. For anions, the quantification limit is 0.016 mg/L with an analytical error of $\pm$ 5 % for Cl and $\pm$ 6 % for SO_4.

Additional cations (Si, Al) were analysed by inductively coupled plasma optical emission spectrometry (ICP-OES) using a Varian 720 ES equipped with an autosampler

Varian SPS-3 and supported by the ICP Expert II Ver. 1.1.2 software and Varian Spectroscopy Database Administrator Ver. 1.6.0.20. For Si and Al, the quantification limit is 0.05 mg/L with an analytical error of ± 7 % for Si and ± 9 % for Al.

Alkalinity and pH were determined using a Metrohm OMNIS Titrator supplied with the OMNIS titration software. Total inorganic and organic carbon concentrations (TC/TIC/TOC) were determined using an Analytic Jena multi N/C 2100S equipped with an infrared NDIR-detector and supported by the Software multiWin (aj). TOC was determined indirectly by analysing the TC and TIC of the sample and calculating the difference. The quantification limits for these technologies are 1 mg/L with an analytical uncertainty of ± 5 (TC, TIC) and 7% for TOC.

1.2.5. Modelling of the batch experiments

Geochemical modelling of the batch experiments was done using PHREEQC (version 3.0, Parkhurst & Appelo, 2013). In a first step, the model was used to assess the initial APWs and calculate the saturation indices for minerals known or assumed to be present in the reservoir rock. In a second step, a kinetic based model of the batch reactions was created using a modified version of example 6 in the PHREEQC manual (version 3.0, Parkhurst & Appelo, 2013). The Thermochimie database (Giffaut et al., 2014) was used. Kinetic reaction rates, consistent with Transition State Theory, for the reacting minerals, were collected from the extensive list compiled by Palandri & Kharaka (2004). Mineral reactive surface areas were not measured but were constrained within limits based on experimental data by Beckingham et al. (2016).

In the model, the artificial porewater was based on the obtained fluid analysis. It was then reacted, whilst being heated to the desired temperature, with the main minerals identified in the rock material. For some model runs, additional changes were made (surface area) to improve the fit between the modelled and experimental data. The model was set up to cover the two weeks the experiments were running. A summary of the model scenarios run can be found in Table 4, Section 1.3.3.3.

1.3. Results

1.3.1. Composition of rock material

Four samples from the Formation des Étiollets were collected (Figure 2), two each from the Complexe Récifal and the underlying Calcaires de Tabalcon . The samples from the Complexe Récifal represent white limestones, while the other two samples are beige-grey and vuggy dolomites.

The mineralogical composition of the four samples is given in Table 3. The two samples from the Complexe récifal were identified as nearly pure limestones composed of

nearly pure calcite. PlaUB1 represent a porous bioclastic limestone made up of a coral framework with shell fragments embedded. Trace amounts of quartz and feldspar are present according to XRD, indicating minimal clastic input into the system. PlaUB2 was classified as a dolomitised limestone in the well log. However, XRD analyses identified only a small amount of dolomite. The sample was therefore reclassified as a micritic limestone. The absence of any clastic minerals (quartz, feldspars, clays) suggests little to no terrigenous input.
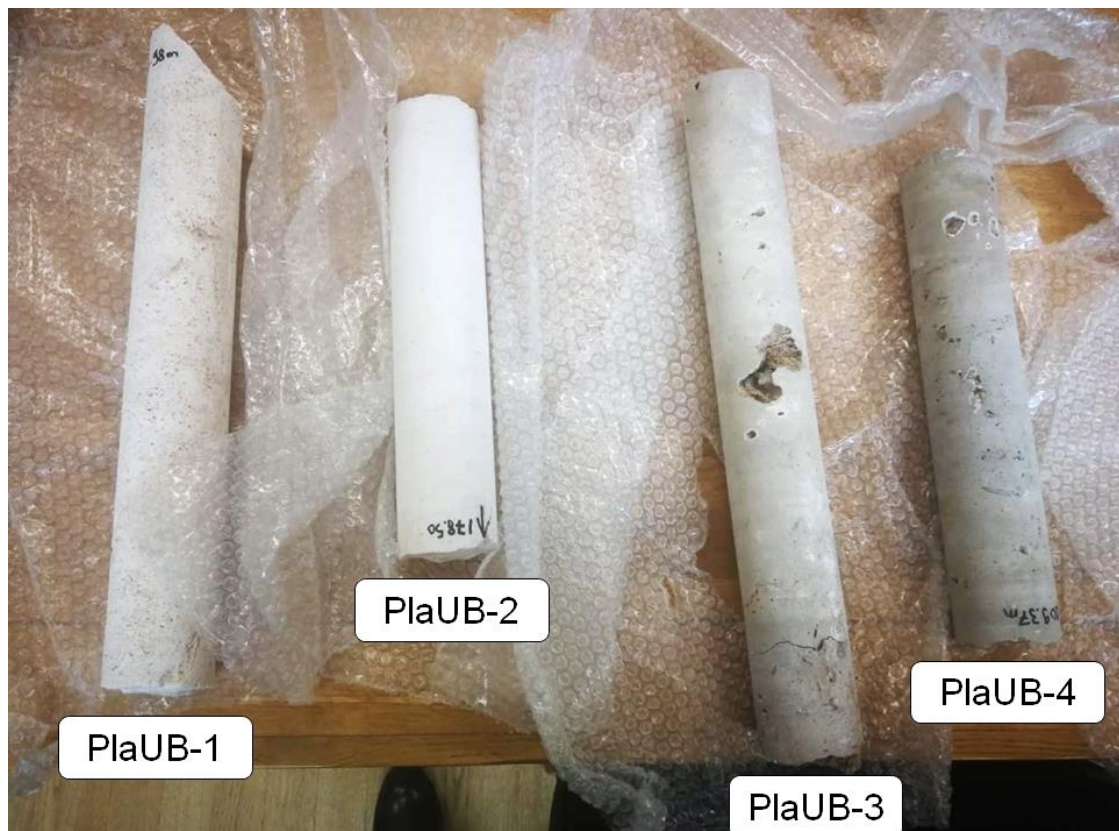

Figure 2: Four rock cores from the Complexe Récifal and underlying Calcaires de Tabalcon, drilled south of Plagne (FR).

The samples from the underlying Calcaires de Tabalcon are both dominated by dolomite. While PLaUB4 is > 90 % dolomite, PlaUB3 also contains 18 wt.% calcite (Table 2) Both show traces of clastic input (quartz in PlaUB3 and feldspar in PlaUB4) and their grey-beige colour suggests the presence of other phases (likely clay minerals) that were not identified by XRD.

In thin sections of PlaUB3, dolomite and calcite are by far the most dominant minerals. The matrix of the sample is made up of dolomite rhombohedra arranged in an idiotopic mosaic. All these crystals showed an inclusion-rich centre. While the inclusions were too small to be identified by petrographic microscopy, they are likely small clastic particles (quartz, feldspars and/or clay minerals). Calcite was primarily present as coarse crystals lining the

vugs, as well as filling the pore space between the dolomite rhombohedra in the area surrounding the vugs (Figure 3). The Fe-content of carbonates can be determined based on their colour (Section 1.2.2.). While the dolomite is Fe-poor (colourless) the calcite crystals often show multiple zonations switching from red (calcite) to purple (Fe-calcite) and back. In sample PlaUB3, hairline fractures are abundant across the sample. During sample preparation, the core generally broke along these fractures, revealing a thin brownish varnish, likely made up of iron hydroxides.
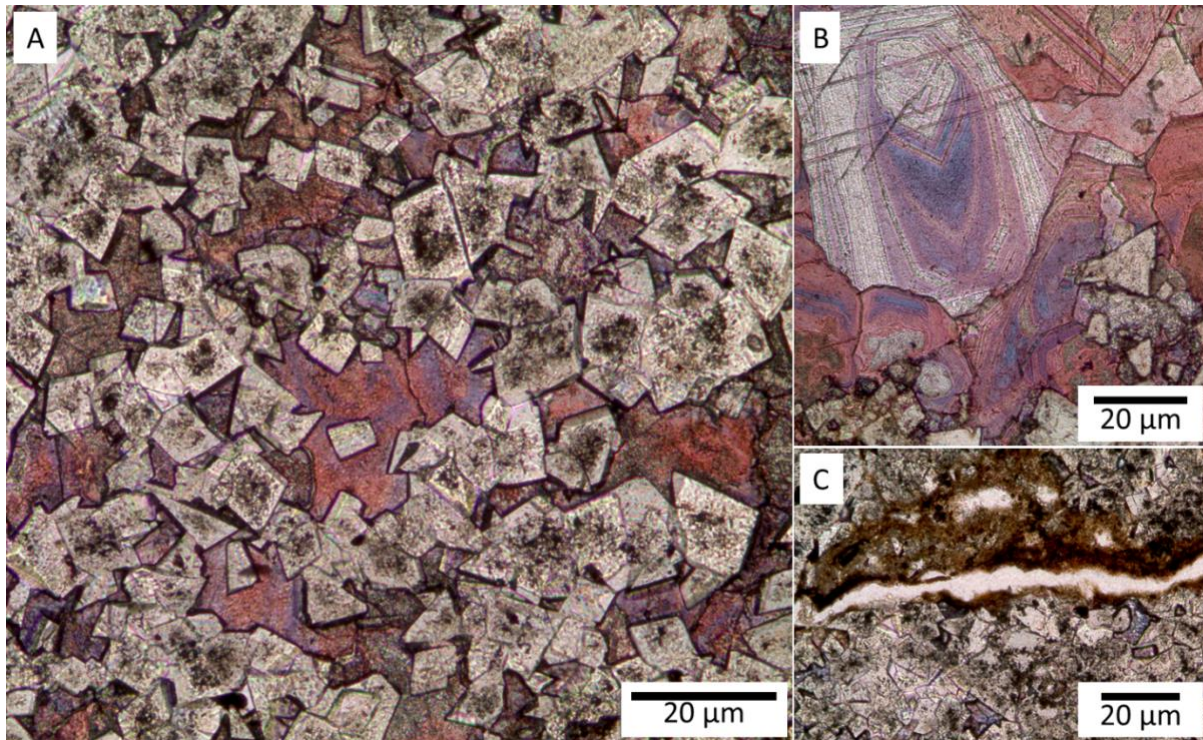

Figure 3: Microphotographs of the artificially stained sample PlaUB-3 showing the matrix made up of dolomite rhombohedra, each with a cloudy centre and clear rim as well as the pore filling calcite showing a zonation between calcite and Fe-calcite (A). The vugs are filled by large (up to 7 mm) calcite crystals which commonly show zonation with calcite and Fe-calcite as well as dolomite (B). A brown, unidentified varnish is lining the abundant fractures (C). Different carbonate minerals stain differently depending on their structure and Fe-content: calcite - red, Fe-calcite – purple and dolomite – colourless (Dickson, 1966).

In addition to the main mineralogy, total organic carbon (TOC), total nitrogen (TN) and total sulphur (TS) content of the samples were also analysed (Table 2). Nitrogen and sulphur were absent in all samples. TOC is very low (< 0.1 wt.%) in the limestones from the Complexe récifal, confirming their pure carbonate nature. The dolomite-rich samples from the Calcaires de Tabalcon on the other hand show TIC values of 0.19 and 0.33 respectively.

For the batch experiments, sample PlaUB3 was selected as it has an abundance of both, calcite and dolomite, which are the two dominant minerals across all Mesozoic carbonates. It also contains the highest TOC content, some clastic input as well as iron hydroxides present. Thus, the mineral reactions are expected to be most diverse and show the most significant changes to the initial APW composition. PlaUB3 is also likely the most challenging sample to predict by geochemical modelling due to the number of concurrent mineral dissolution and precipitation reactions controlled by or competing for ions in solution.

Table 2. Description of each rock sample taken from the complexe Récifal and underlying Calcaires de Tabalcon.

	Stratigraphy	Lithologies		Mineralogical composition (in wt.%)				TOC[1] (wt.%)
		Well profile	Petrography + XRD analysis	Cc	Dol	Qtz	Fsp	
PlaUB1	Complexe récifal	Bioclastic limestone	Porous bioclastic limestone	100		<1	<1	0.05
PlaUB2		Dolomitised limestone	Micritic limestone	99	<1			0.07
PlaUB3	Calcaires de Tabalcon	Dolomite	Vuggy dolomitised limestone	18	82	<1		0.33
PlaUB4			Vuggy dolomite	4	94		<1	0.19

[1]*Total nitrogen and total sulphur were measured but are absent (0.000 wt.%) in all four samples.*

1.3.2. Composition of APW

The APW was replicated from Table 1 using the method outlined in Section 1.2.2. A new batch was prepared for each experiment, including one each for the two-part 60 °C experiment. All APW analyses are shown in Table 3. The APW was bubbled with an Ar/CO_2 gas mix at pCO_2 $10^{-2.2}$ to increase the pressure of CO_2 in solution to resemble reservoir conditions *(Section 1.2.2).* To check this was successful for each of the analysed APW mixtures saturation indices at 25°C were calculated in PHREEQC. The resulting pCO_2 of each APW was between 10^{-2} and $10^{-2.2}$. Adjustment of the pCO_2 was therefore successful and degassing between bubbling and analysis was minor.

Table 3. Analysis of all 4 APWs constructed, emulating the composition of groundwater sampled from the Geo-2 borehole, Calcaires du Tabalcon Formation.

		20 °C	60 °C a	60 °C b	90 °C
pH$_{sampling}$	-	7.58	7.26	7.28	7.28
pH$_{lab}$	-	7.55	7.77	7.47	7.47
logp_{CO_2}		-2.19	-2.03	-1.74	-1.48
Concentration of Ions					
Na	mmol/L	2.24± 0.135	2.24± 0.135	2.24± 0.135	2.24± 0.135
K	mmol/L	0.08± 0.007	0.20± 0.018	0.08± 0.007	0.08± 0.007
Ca	mmol/L	0.89± 0.053	0.89± 0.053	0.89± 0.053	0.89± 0.053
Mg	mmol/L	0.60± 0.024	0.62± 0.025	0.61± 0.024	0.60± 0.024
Al	mmol/L	0.00	0.00	0.00	0.00
Si	mmol/L	0.02± 0.001	0.01	0.00	0.02± 0.001
Cl	mmol/L	2.28± 0.114	2.35± 0.118	2.39± 0.119	2.28± 0.114
SO$_4$	mmol/L	0.32± 0.022	0.35± 0.025	0.35± 0.024	0.32± 0.022
HCO$_3$	mmol/L	2.25± 0.112	2.25± 0.113	2.24± 0.112	2.25± 0.112
TOC	mg/L	1.4± 0.098	6.5± 0.455	n/a	n/a
TIC	mg/L	31.8± 1.59	30.0± 1.5	n/a	n/a
SI of Phases					
Calcite		-0.56	0.03	-0.26	-0.07
Dolomite		-1.15	0.34	-0.25	0.33
Quartz		-0.93	-1.94	-3.2	-1.66
K-feldspar		-1.99	-5.44	-8.63	-6.22
Muscovite		-2.96	-2.72	-3.36	-5.35
K-Montmorillonite[1]		-1.88	-6.71	-10.08	-6.52

[1]All other smectites in the database are also undersaturated in solution.

1.3.3. Experimental results

The batch experiments were run using powdered PlaUB3 rock material at 20, 60 °C and 90 °C. The vessels were sampled in duplicates at six timesteps over 13 days, providing time-resolved data on the evolution of fluid composition. The measured composition and the initial APW composition were used to calculate the net gain/loss of ions at the end of the experiments (Figure 4). A net gain represents the addition of the element through mineral dissolution, while a net loss represents removal by mineral precipitation. After 13 days, we see significant increases of silicon, potassium, aluminium and magnesium (Si, K, Al and Mg) ions in solution along with a decrease in Calcium (Ca) (Figure 4) at all temperatures. Changes in sodium, chloride and sulphate (Na, Cl and SO$_4$) concentrations all occur within the analytical errors, meaning no significant change in concentration of these ions occurred.
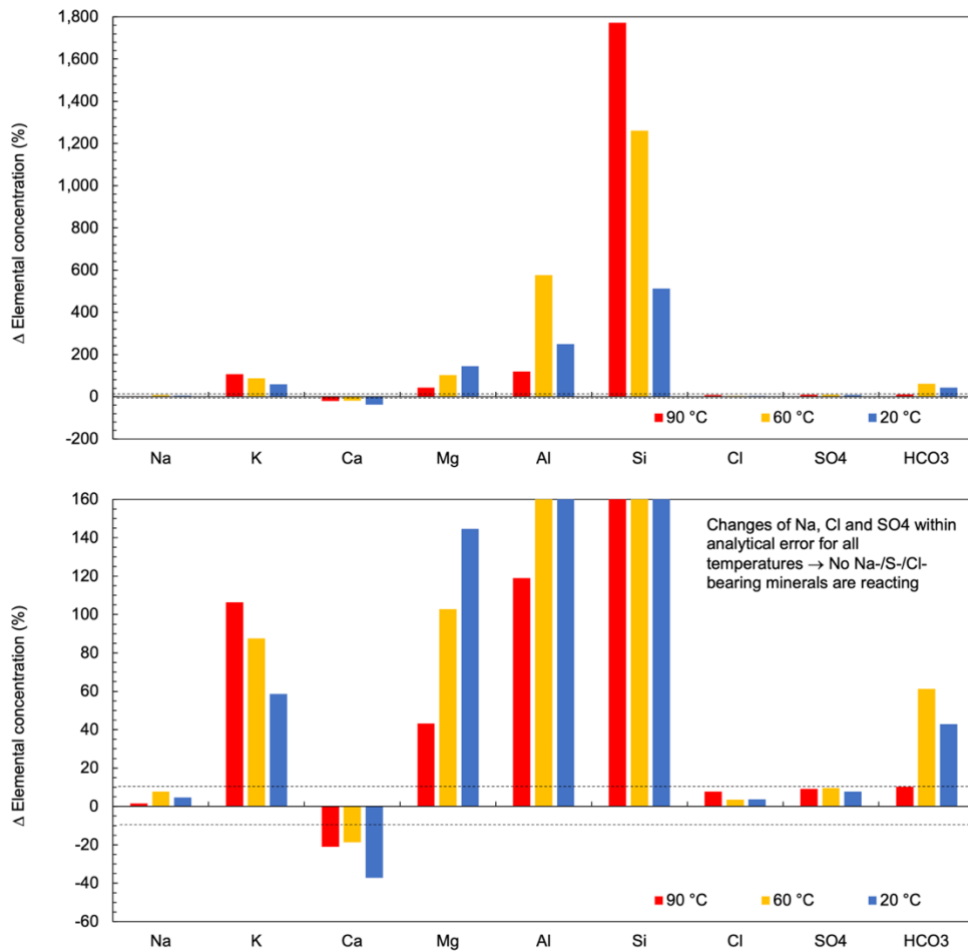
Figure 4: Net loss/gain of major solutes (in mol%) in the pore water after the duration of the batch experiments (13 days) at 20, 60 and 90 °C. A decrease is indicative of precipitation of a phase containing that solute; an increase is indicative of dissolution. The dotted horizontal lines show the uncertainties in the original solute concentrations. Both panels show the same data but different x-axes.

As all elements can be involved in the dissolution and/or precipitation of multiple minerals, none of the observed changes can be associated reliably with a single mineral reaction. However, different elements are likely associated with different minerals groups. Changes in calcium and magnesium concentrations are likely dominated by carbonate reactions while the other elements require the involvement of (alumo)silicates. A more detailed understanding can be gained by investigating the evolution of elemental concentrations as a function of time (Figure 5) and combining the resulting observations with knowledge of the saturation state of potential minerals present in the APW (Table 3).

With dolomite and calcite being the dominant minerals present in the sample, reactions of these minerals can be inferred to explain observed changes in the concentration of magnesium (Mg) and calcium (Ca). Magnesium shows a logarithmic-type increase as a function of time (Figure 5). The extent of the concentration increase of magnesium decreases with increasing temperatures (Figure 4 and 5). At 20 °C concentration of magnesium increases by 0.8 mmol/L (141%); this is reduced to an increase of 0.6 mmol/L (105%) at 60 °C and then just 0.2 mmol/L (33%) at 90 °C. At 90 °C, the concentration of Magnesium in solution has reached equilibrium with the concentration curve flattening off after approximately 10 days. At lower temperatures this is not the case, with a continued increase still apparent after 13 days at both 60 °C and 20 °C.

Magnesium is contained in dolomite, micas, clay minerals and chlorites. Dolomite is the only of these minerals which is abundant according to XRD (Table 2) and its retrograde solubility is in line with the reduced increase at higher temperature. Thus, dolomite dissolution is the most likely process to explain the observed magnesium increase. However, at elevated temperatures, the initial APW is supersaturated with respect to dolomite. Despite this, we propose that the observed increase is due to dolomite dissolution. This is due to the kinetic inhibition of dolomite precipitation. Precipitation of dolomite at ambient temperature is considered virtually impossible, requiring geological time scales to occur (Deelman, 2011; Gregg et al., 2015; Kaczmarek & Thornton, 2017). The limitation has primarily been attributed to the strong solvation shells of magnesium ions in aqueous media (Xu et al., 2013; German Montes-Hernandez et al., 2016). Previous attempts to synthesise dolomite at temperatures of 60 and 90 °C showed that it takes seven and three years respectively (Usdowski, 1989). Geochemical models (like the one used in this study) determine whether a mineral will precipitate or dissolve based on the SI of the mineral in question. In practice, dissolution still occurs when a mineral is supersaturated (SI>0) just at a lower rate than precipitation. Therefore, when precipitation is kinetically inhibited, as it is for dolomite under the conditions here, dissolution will still be occurring even when it is saturated in solution, leading to the observed increase in magnesium.

The calcium ion (Ca) is the only ion measured in solution to show a marked decrease in concentration at all temperatures (Figure 4). The decrease in calcium concentration is greater at 20 °C than at 60 and 90 °C. The decrease in concentration at these two higher temperatures is similar, decreasing by 0.18 and 0.14 mmol/L at 90 and 60 °C, respectively (a 20-21% decrease). Concentration decreases by 0.3 mmol/L at 20 °C, a 60% decrease. At 20 °C the decrease is continuous while at 60 and 90 °C, an increase is observed in the first day, followed by a decrease for 2 days before a steady state is reached around 4 days.
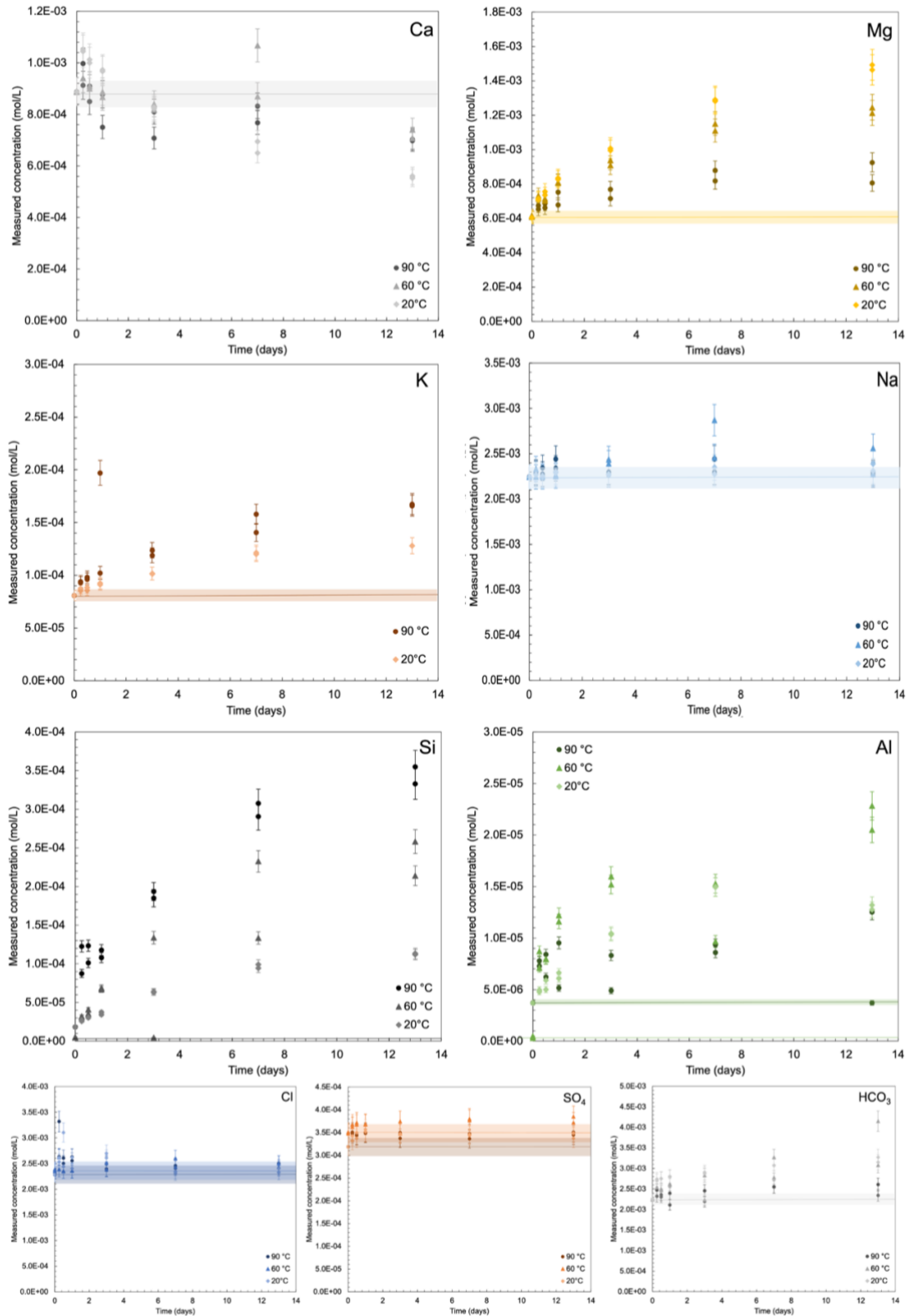
Figure 5. Concentration over time for each major ion analysed from the APW throughout the duration of the batch experiments run at 20, 60 and 90°C. Boxes indicate the analytical uncertainties. If a measured concentration value falls within the box, it is within the error of the starting concentration measurement, indicating no observable change in concentration. Time-resolved data for potassium concentrations were not available at 60 °C due to an error in preparing the porewater.

Calcium can be incorporated into carbonates, plagioclase and a number of sheet silicates. While we did not investigate the composition of the rock material after the experiments, the precipitation of calcite explains why we observe an initial increase in calcium concentration. The initial APW is undersaturated with respect to calcite (Table 3), resulting in a small amount of calcite dissolving until saturation is reached. The subsequent decrease in concentration is related to the release of calcium from dolomite dissolution (see above) which results in the precipitation of calcite and a net removal of calcium from solution. This removal is greater at lower temperatures due to the higher dissolution of dolomite at lower temperatures due to its retrograde solubility.
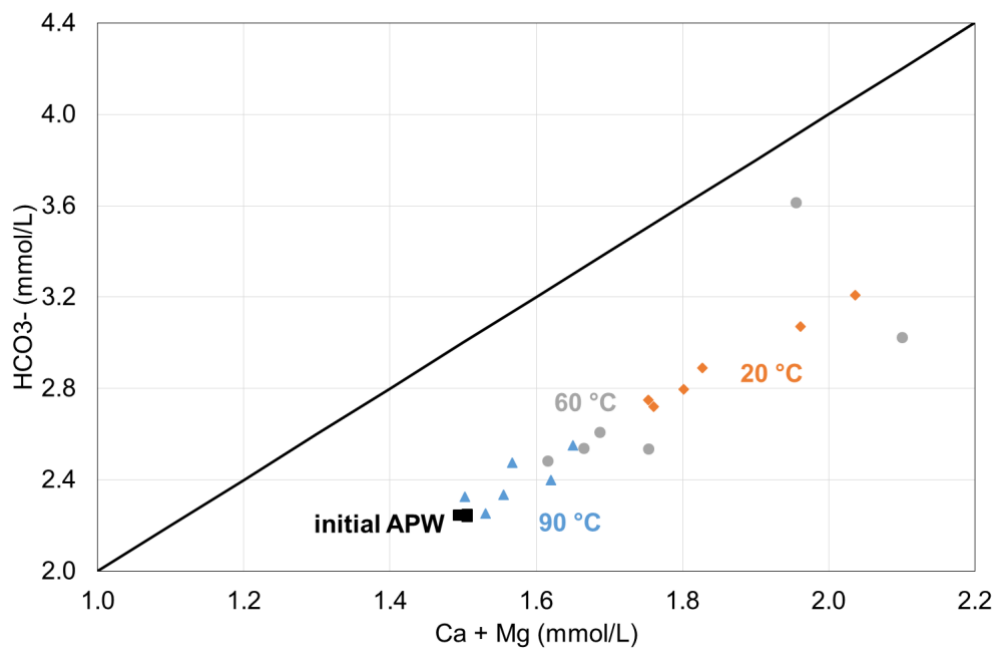

Figure 6: Water hardness (Mg+Ca concentration) versus bicarbonate concentration in solution. When the solution composition is controlled by carbonate dissolution and/or precipitation alone, the experimental data points should evolve along a linear trend parallel to the indicated line (ratio 2:1 bicarbonate- Mg+ Ca). Our experiment data follow this expected trend.

In order to assess if only carbonate minerals are responsible for the observed changes in magnesium and calcium concentrations or if silicate minerals are involved as well, we plotted the Mg + Ca concentrations versus the measured bicarbonate concentrations for all solutions analysed (Figure 6). All waters in a pure carbonate system should fall onto the 1:2 ratio line ("carbonate line", Figure 6). The compositions of the initial APW plot at a ratio lower than 1:2, suggesting that the reservoir groundwater is affected by other processes, most likely mixing with a groundwater from a different source. However, all the time-series aliquots plot on a line parallel to the carbonate line going through the initial APW concentration,

suggesting that only carbonate mineral reactions are responsible for the observed changes and no silicate minerals are involved.

1.3.3.2.   Silicate reactions

Despite the XRD results showing that silicate minerals are all but absent (Table 2), we see an increase in potassium (K), silicon (Si) and aluminum (Al) over the course of the experiments. All show similar trends at all temperatures with a logarithmic-type increase in their concentrations (Figure 5). This increase is more substantial at higher temperatures (Figure 4). Unlike the other two ions, aluminium shows a far greater increase in solution at 60 °C (0.02 mmol/L) rather than at 90 °C (0.004 mmol/L). However, the concentrations of aluminium in solution are very low and will therefore not be discussed any further. The concentrations of both potassium and silicon do not reach steady state over the two weeks of the experiment.. Over 13 days, concentrations of potassium increased by ~107% at 90 °C and ~58% at 20 °C. The concentration of silicon in solution shows the largest increase of all the analysed ions (Figure 3). Starting at a concentration of effectively 0 mmol/L silicon in solution, the ion increases to 0.33 mmol/L (or 9.4 mg/L) at 90 °C, to 0.25 mmol/L at 60 °C and to 0.13 mmol/L at 20 °C.

The increase of potassium, silicon and aluminium ions in the porewater over time indicate addition through the dissolution of (alumo)silicate minerals. Common silicate minerals that could influence the concentrations of these elements in solution are quartz (Si only), albite (Si and Al), as well as K-feldspar, micas, illites and smectites (Si, Al and K). Based on speciation calculations of the initial APW (Table 3), all of these phases are undersaturated and could therefore dissolve, raising concentrations of their constituent ions. These minerals exhibit normal prograde solubility, meaning that they are more soluble at higher temperatures. This is in line with the observed higher concentrations of silicon and potassium in solution with increasing temperatures. Based on XRD analyses (Table 2), quartz was identified in the reacting PlaUB3 rock. However, the similarly shaped curves of silicon and potassium are indicative of linked dissolution behaviour, suggesting the involvement of a non-identified K-bearing alumosilicate. Due to the high analytical uncertainty of XRD analyses, phases with very low abundances are notoriously difficult to quantify, even identify, by XRD. It is therefore probable that silicate minerals other than quartz are present in PlaUB3. In thin section analysis, small but abundant mineral inclusions inside the dolomite rhombohedra were observed. While we could not identify them, they are likely the missing K-bearing alumosilicate. K-feldspar is a likely candidate, especially as it was identified by XRD in sample PlaUB4 (Table 2) but other sheet silicates could be present as well. In order to better constrain the silicate minerals present, the time-resolved concentrations were modelled.

1.3.3.3. *Kinetic modelling*

Based on the solution compositions and considerations of saturation states, several mineral reaction have been identified so far. In order to check these interpretations (carbonate minerals) and narrow down potential mineral reaction further (silicates), kinetic models were run to replicate the concentrational trends observed in the 20 and 90°C experiments (Section 1.3.3.1, 1.3.3.2). The scenarios run are described below in Table 4.

Table 4. The Different PHREEQC model scenarios run throughout the study using the method described above.

Element to be fitted	Temperature (°C)	Base model	Additional changes
Ca			Surface area
Mg			Surface area
Si	20, 60, 90	cc (dissol. and ppt), dol (dissol only), qtz (dissol only)	Surface area, K-feld (dissol. and ppt), K-mont (dissol. and ppt), limiting conc
K			Surface area[1], K-feld (dissol. and ppt), K-mont (dissol. and ppt)
Na			none

[1]only at 20 °C

The first model run was used to assess evolution of magnesium and calcium concentrations based on the base model (Table 4). Without modifications, initial calcite dissolution and the corresponding calcium increase is observed (see above) but after 1 day no more concentrational changes can be seen. In order to replicate the observed magnesium increase, continued dolomite dissolution was thus implemented. This resulted in an increase in magnesium and a decrease in calcium due to the resulting precipitation of calcite (Figure 7). The surface area (reaction rate) of dolomite was modified here to achieve the best fit of the model to the experimental data within reason (Beckingham et al., 2016). The fast reaction rate is more in line with the initial trend of increase of concentration, whilst the slower fits the general trend of the entire reaction. At 90 °C them magnesium increase slows down, and a steady state is reached after around a week. This behaviour cannot be replicated by a model assuming continuous dolomite dissolution. A likely reaction taking place decreasing the magnesium concentration in the later stages of the experiment is the precipitation of an unidentified, likely poorly crystalline or amorphous Mg-(alumo)silicate. Such phases have been synthesised in the laboratory as well as observed in Icelandic district heating systems under similar chemical conditions and temperatures over the course of a few hours (Harder, 1972; Gunnlaugsson & Einarsson, 1989; Hauksson et al., 1995). In addition, the same process

was used to explain the observed magnesium concentrations in the batch experiments done for the Forsthaus cores (van den Heuvel et al., 2021).
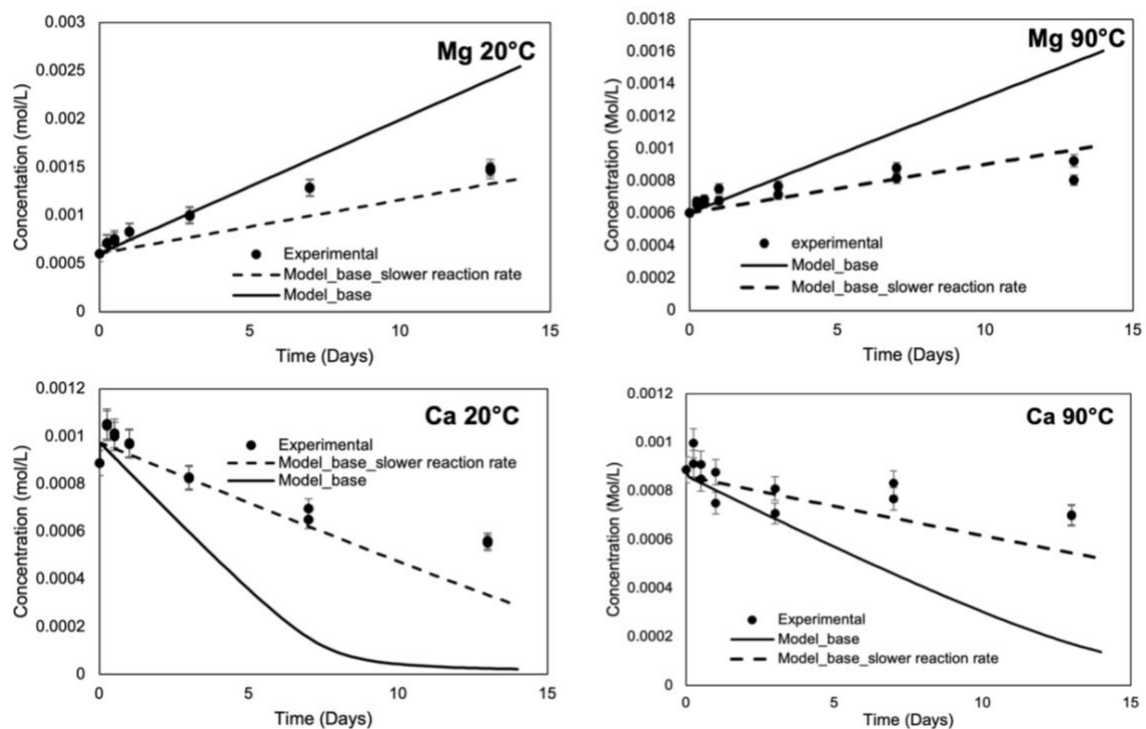

Figure 7. Magnesium and calcium concentrations in the batch experiment solutions as a function of time (dots). The kinetic PHREEQC models (lines) attempt to replicate the observed evolution at 20 and 90 °C. The two lines show different rates of dolomite dissolution: black fast, dashed slow.

Besides dolomite and calcite, the base model also includes quartz, which dissolves throughout the experiment as it remains undersaturated. This allows for a good fit of the experimentally observed silicon trends. The fit is further improved when the reaction rate is adjusted slightly by changing the surface area of quartz (Figure 8A&B). However, to explain the observed increase in potassium concentrations, additional K-bearing alumosilicates need to be included in the model. Potential phases are K-feldspar, muscovite, illite and K-smectites, all of which are common clastic components. K-feldspar is the most soluble of these minerals. By including it in the model and adjusting the surface area (= reaction rate) slightly, a good fit was obtained for the K concentrations at 90 °C (Figure 8D). Other K-bearing mineral phases are less soluble. Their inclusion in the model leads to a strong underestimation of the potassium concentrations (K-montmorillonite shown as an example, Figure 8C&D). The same is true for K-feldspar dissolution at 20 °C (Figure 8C). So far, we do not have a satisfactory explanation for this behaviour. It is possible that the potassium increase at 20 °C is controlled by another, even more soluble mineral phase not identified or that the database entry for one or several of the sheet silicates underestimates reaction rates. It is also possible that the very

fine-grained nature of the inclusions which are the likely source of potassium (Figure 3) results in high surface areas which are outside the limits outlined by Beckingham et al. (2016) and were thus not considered in our models.
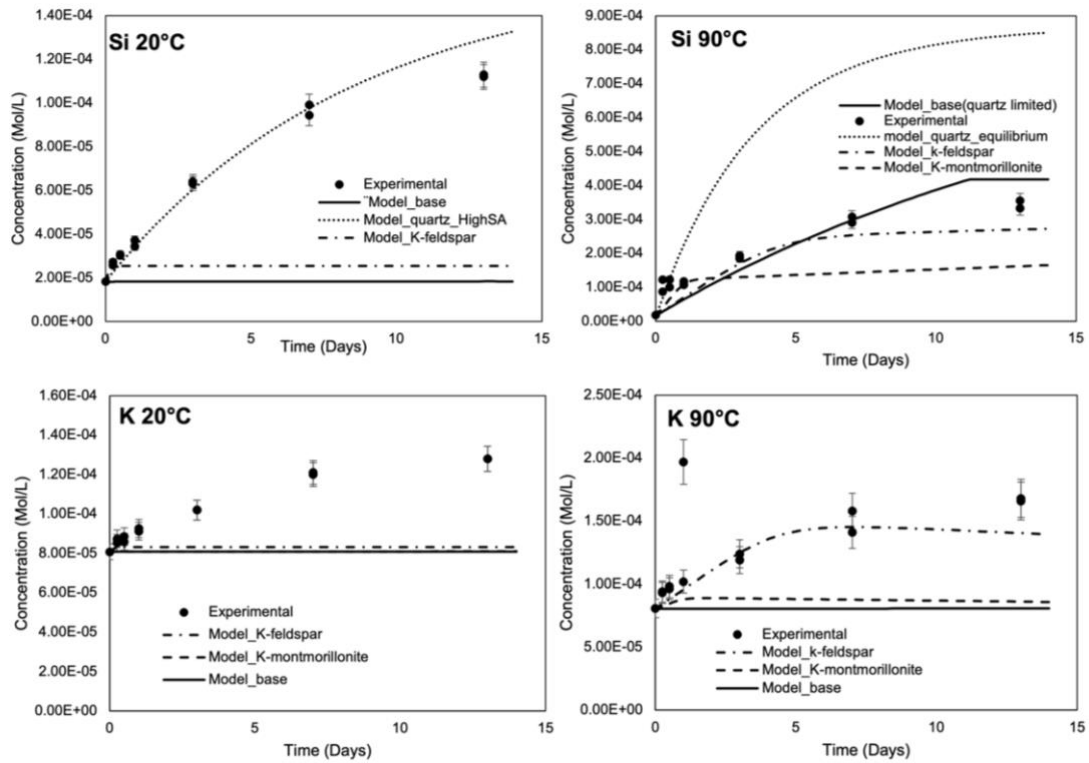

Figure 8: Silicon and potassium concentrations in the batch experiment solutions as a function of time (dots). The kinetic PHREEQC models (lines) attempt to replicate the observed evolution at 20 and 90 °C. The continous black lines represent the base kinetic PHREEQC model (Section 1.4). The dotted lines additionally modify the reaction rate of quartz to much higher values than presented in Beckingham et al. (2016). Dashed lines take into account the addition of other phases (K-feldspar, K montmorillonite).

2. Corrosion and scaling in the GEo-01 well during shut-in

2.1. Background

Downtimes when no fluid flow occurs are common during operation of HT-ATES systems. Such downtimes when the wells are shut in have previously been identified as periods of active damage to the systems (or at least individual components such as wells). This is attributed to corrosion due to either O_2 ingress during maintenance or to microbial activity.

This effect has been studied in detail at the operating HT-ATES in Neubrandenburg (Westphal et al., 2016). That study evaluated the change in chemical as well as microbial parameters after well shut-ins of up to three months. They found that the microbial activity (incl. biofilm formation) and diversity substantially increased (incl. sulphur-oxidising bacteria, SOB) during the downtime. This is likely attributed to better growth conditions (e.g. higher DOC) and lack of removal of cells by the passing fluid. Corrosion and formation of Fe-sulphides strongly increased on the cold side of the system due to higher populations of bacteria and to the presence of SOB, which produce sulphuric acid as part of their metabolism.

Indications from previous sampling campaigns at the GEo-01 well suggest similar processes. In 2019, it was observed that the water produced from the geothermal GEo-01 well contained a black-coloured suspended particle load after the well had been shut in for several weeks prior to production (Figure 9). A preliminary study suggested that the colour is due to pyrite that precipitated during the corrosion of the steel casing (Güntert, 2020). To test this hypothesis and to elucidate the governing processes driving corrosion, we have carried out a time dependent sampling of both the produced water and the suspended load in June 2020 after the well had been closed for more than 3 months due to Covid-19 restrictions. Both sample types were analysed for their chemical and sulphur isotopic compositions. In addition, microbial analyses were carried out to assess the role of microbes during the potential corrosion of the casing.

Figure 9: Wellhead of GEo-1 producing thermal water containing a black-coloured suspended load.

2.2. Methods

2.2.1. Sampling

The GEo-01 well is 750 m deep and produces thermal water from the lower Cretaceous and upper Jurassic carbonate aquifers under artesian conditions at a rate of 50 L/s at 32 °C (Guglielmetti et al., 2020). During the first Covid-19 shutdown in spring 2020, the well had been closed for more than three months from February 25 to June 9 2020. When it was reopened on June 9, water, suspended load, and microbial samples were collected after producing for 2, 9, 16, 36, and 136 minutes at 35 L/s. Each sample thus refers to a particular location along the GEo-01 well or the adjacent reservoir. To better illustrate this, results from geochemical and microbial analyses will be shown as a function of the produced well volume (1 well volume = 73'500 L). During sampling, the production rate was reduced to less than 1 L/s.

To collect water samples, the produced thermal water was filtered at 5 μm using two in-line polypropylene wound filters connected to the outflowing tube. At each point in time, several water aliquots were taken. The ones foreseen for the analysis of total concentrations of H_2S were taken under anoxic conditions using glass bottles filled below the water table of a 10 L water bucket. Aliquots for ion chromatography (IC) as well as optical emission spectroscopy (OES) analyses were additionally filtered at 0.2 μm using polyethersulfone (PES) syringe filters from Millipore and transferred into 60 mL polypropylene bottles. Cations and metals were conserved by acidifying the corresponding bottles to pH ~ 2 using HNO_3. 5 L canisters pre-filled with ca. 50 g of Cd-acetate powder were filled to obtain aliquots for sulphur and oxygen isotope analysis of dissolved SO_4 and H_2S. The pH and water temperature were measured on-site using a Hamilton pH electrode in combination with a Knick field measurement device.

Suspended load samples were obtained by filtering the thermal water bypassing the wound filters at 0.22 μM using a vacuum pump in combination with mixed cellulose esters membrane filters from Millipore. Suspended load concentrations were determined by tracking the filtered water volume and measuring the weight difference of the filters before and after filtration.

Samples for microbial analysis were filtered at 0.45 μm using single-use, sterile DNA filtration units based on cellulose nitrate from Fisher Scientific. The filters were frozen on-site at -78.5°C using dry ice and immediately shipped to GFZ Potsdam. Upon arrival at GFZ in the frozen state, the filters were stored at -80°C prior to analysis.

2.2.2. Analytical techniques

2.2.2.1. Chemical water analyses

Concentrations of major cations (Na^+, K^+, Ca^{2+}, Mg^{2+}) and anions (Cl^-, F^-, SO_4^{2-}) were determined at the Institute of Geological Sciences, University of Bern by IC using a Metrohm ProfIC AnCat MCS IC system with automated 5 μL and 50 μL injection loops. Total inorganic and total organic carbon concentrations were determined using a TIC/TOC analyser (Analytic Jena multi N/C 2100S) with a detection limit of 0.1 mg/L. Concentrations of Fe_{tot} were also analysed at the University of Bern by optical emission inductively coupled plasma spectrometry (ICP-OES) using a Varian 710 ES ICP-OES system with a detection limit of 0.01 mg/L.

Total hydrogen sulphide concentrations (H_2S_{tot}) were determined at Hydroisotop GmbH by UV/Vis spectroscopy using a Spectroquant spectrophotometer from Merck. The analytical error of all techniques was better than ± 5% based on multiple measurements of high-grade, commercial standard solutions.

2.2.2.2. Chemical and structural analyses of suspended load samples

The mineralogical composition of the suspended load samples (Figure 10) was qualitatively determined by X-ray powder diffraction (XRD) at the Institute of Geological Sciences, University of Bern using a Panalytical X'Pert Pro diffractometer. For analysis, the filters used to collect the suspended load were fixed into sample holders using aluminium plates. The chemical composition of the suspended load was semi-quantitatively determined at the University of Bern by analysing the filters using a desktop MiniPal2 X-ray fluorescence spectrometer from Philips.

Mössbauer spectrometry was employed at the Institute de Molécules et Matériaux (IMMM) at Le Mans University to measure the iron oxidation states of the suspended load samples and to identify Fe bearing phases present. The spectra were recorded at room temperature (300 K) and at 77 K using a constant acceleration transducer and a ^{57}Co source dispersed in a Rh matrix. Velocity calibrations were carried out using an α-Fe foil at room temperature.

Figure 10: Filtered samples of suspended particle loads collected after producing for 0.04, 0.24, 0.44, 1.01, and 3.87 well volumes (from left to right). The colour difference relates to a variation of the

dominating iron-bearing phase (Table 5). The rusty colour of the first sample reflects the presence of nanocrystalline Fe^{3+}-bearing oxy-hydroxides, whereas the grey colour of the other samples is due to Fe^{2+}-bearing pyrite.

2.2.2.3. *Sulphur and oxygen isotope analysis*

The sulphur and oxygen isotope composition of sulphate and hydrogen sulphide dissolved in the thermal water samples ($\delta^{18}O_{SO4}$, $\delta^{34}S_{SO4}$, $\delta^{34}S_{H2S}$) was determined at Hydroisotop GmbH by isotope ratio mass spectrometry (IRMS). The analytical error (1σ) was better than 0.5 ‰.

The sulphur isotope composition of the suspended load samples was also determined at Hydroisotop GmbH by heating the filters used to collect the suspended load followed by isotope ratio mass spectrometry (IRMS) of the evaporated samples. The analytical error (1σ) was better than 0.3 ‰.

2.2.2.4. *Microbial analysis*

DNA extraction and PCR amplification of the filtrate was conducted at GFZ Potsdam. Subsequently, the microbial community was identified and quantified by DNA sequencing carried out at a commercial sequencing facility in Aarhus, Denmark.

2.2.3. Geochemical modelling

Geochemical modelling was conducted using PHREEQC V3 (Parkhurst and Appelo, 2013) in combination with the Wateq4f database to (i) calculate the saturation indices of calcite and dolomite in the collected thermal water samples and (ii) to model corrosion as well as calcite scaling scenarios.

2.3. Results

2.3.1. Chemical and isotopic composition of water and suspended load samples

The chemical and sulphur isotope composition of the thermal water sampled from GEo-1 as a function of time is listed in Table 5. With the exception of dissolved sulphur species (SO_4, S_2O_3, H_2S), the chemical composition was very constant over the sampled production period. Figure 11a demonstrates that all sulphur species showed a general increase with increasing production time. The concentrations of oxidized sulphur species (S_2O_3, SO_4), however, reached a short-term, temporal maximum after the production of 0.2–0.5 well volumes, while the H_2S concentration increased continuously. In addition, the first sample taken after two minutes displayed a higher pH and lower concentrations of Ca and HCO_3^- than all other samples. As a consequence, the CO_2 partial pressure was significantly lower for this sample.

Likewise, it was the only sample showing a significant supersaturation with respect to calcite and dolomite (saturation index SI >> 0.0). All other samples were close to saturation with respect to both carbonate phases.

The temporal maximum in oxidized sulphur species concentrations coincides with the maximum of the suspended load concentration (Figure 11b). XRF and XRD analyses demonstrate that the suspended load did not show large compositional variations and consisted of quartz, clay minerals, and iron-bearing phases. In contrast, carbonates were mostly absent (Figs. 4,5). Thus, the composition of the suspended load samples significantly differed from that of the carbonate reservoir aquifer.

For the sample taken after two minutes, nanocrystalline Fe^{3+}-bearing oxy-hydroxides were identified as the only Fe-phases based on Mössbauer spectroscopy. In contrast, pyrite (Fe^{2+}-bearing, FeS_2) was identified as the dominating Fe-phase present in all other suspended load samples (Figure 14, Tables 5, 6). The strong colour difference of the suspended load samples (Figure 10) thus relate to the variation of the oxidation state of the dominating iron-bearing phase.

The sulphur isotope composition of both the suspended load (i.e. mainly pyrite) and sulphate dissolved in the thermal water showed a clear trend of decreasing $\delta^{34}S$ values with increasing production time (Table 5). Interestingly, most of the $\delta^{34}S$ values of both the suspended load and sulphate dissolved in thermal water samples follow a Rayleigh fraction model (Figure 15)

$$\delta^{34}S = \left(\delta^{34}S_{Ini} + 1000\right) \cdot f^{(\alpha-1)} - 1000 \qquad (1)$$

where $\delta^{34}S_{Ini}$ refer to the $\delta^{34}S_{H2S}$ and $\delta^{34}S_{SO4}$ values of the sample with the highest total sulphur concentration observed after having produced for 3.9 well volumes (17.1 and 18.8‰), f is the remaining H_2S fraction in the thermal water with respect to the maximum concentration observed after having produced for 3.9 well volumes (3.9 mg/L), and α is the sulphur isotope fractionation factor set to 0.9983 corresponding to an enrichment factor ε of -1.7 ‰ ($\varepsilon = (\alpha-1)\times1000$). Such Rayleigh type behaviour is observed if stable isotope fractionation occurs during a single kinetic process where the reaction product does not interact with the reactant (Wiederhold, 2015). Thus, the observation that the samples taken after the production of 0.04 (suspended load sample; $\delta^{34}S_{H2S}$ = 19.4‰) and 0.2 well volumes (thermal water; $\delta^{34}S_{SO4}$ = 22.4‰) did not follow the same Rayleigh fractionation model demonstrates that multiple processes involving sulphur species are occurring within the GEo-1 well.

Table 5: Geochemical data collected for the GEo-01 well on June 9, 2020.

Parameter	Unit	GEo-01-1	GEo-01-2	GEo-01-3	GEo-01-4	GEo-01-5
Production time	min	2	9	16	36	136
Produced well volume	-	0.04	0.24	0.44	1.01	3.87
Temp. (°C)	°C	17.6	28.4	29.9	31.9	32.7
pH	-	8.80	7.80	7.78	7.62	7.73
Eh	mV	-327	-275	-278	-275	-281
Na^+	mg/L	33.1	32.9	33.0	32.9	32.7
K^+	mg/L	2.6	2.4	2.4	2.4	2.4
Ca^{2+}	mg/L	18.8	28.1	28.1	28.3	28.1
Mg^{2+}	mg/L	13.3	14.3	14.2	14.2	14.2
Sr^{2+}	mg/L	2.38	2.59	2.58	2.63	2.61
Fe	mg/L	0.23	0.03	0.04	0.03	<0.02
Cl^-	mg/L	10.1	9.8	9.8	9.9	9.9
F^-	mg/L	0.10	0.14	0.29	0.55	0.66
SO_4^{2-}	mg/L	<0.04	6.30	9.66	0.62	10.74
$S_2O_3^{2-}$	mg/L	<0.04	4.90	0.04	3.72	0.04
H_2S tot	mg/L	< 0.1	2.1	2.5	3.4	3.9
HCO_3^-	mg/L	178	209	210	208	208
TOC	mg/L	2.22	1.94	2.44	2.53	2.22
$\delta^{34}S_{SO4}$	‰	i.p.	22.4	19.2	i.p	18.8
$\delta^{18}O_{SO4}$	‰	i.p.	i.p.	2.9	i.p	7
$\delta^{34}S_{H2S}$	‰	i.p.	i.p.	i.p.	i.p.	i.p.
Suspended load concentration	mg/L	19.9	40.5	76.2	13.4	16.5
Dominating Fe phase		Fe^{3+} oxy-hydroxides	Pyrite	Pyrite	Pyrite	Pyrite
$\delta^{34}S_{SuspendedLoad}$	‰	19.4	18.5	18	17.2	17.1
Saturation index of calcite		0.75	0.17	0.17	0.04	0.15
Saturation index of dolomite		1.02	-0.08	-0.06	-0.28	-0.05
Log(p_{CO2})		-3.64	-2.48	-2.44	-2.28	-2.38

n.m.: not measured;

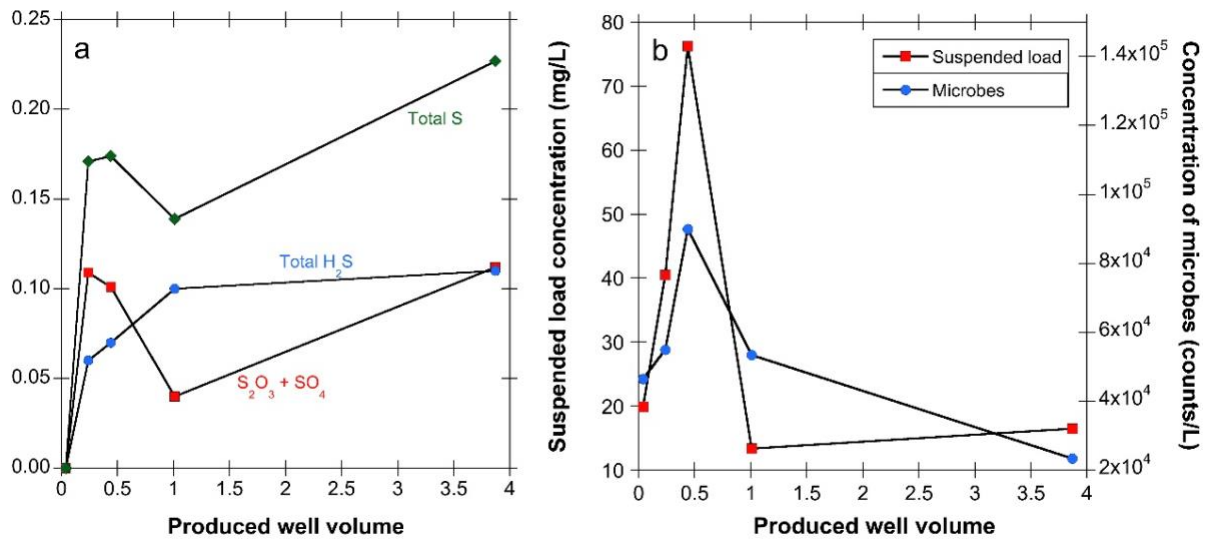*i.p..: impossible to measure (Sulphate conc. too low)*

Figure 11: Concentrations of (a) dissolved sulphur species and (b) the suspended particle load as well as microbes as a function of the produced well volume (1 volume = 73500 L). Note that the produced well volume is a proxy of the location of the corresponding water samples along the depth of the GEo-01 well and in the nearby reservoir. In other words, produced well volumes smaller than one refer to water samples taken within the well, whereas produced well volumes greater than one refer to samples originating from the adjacent aquifer.
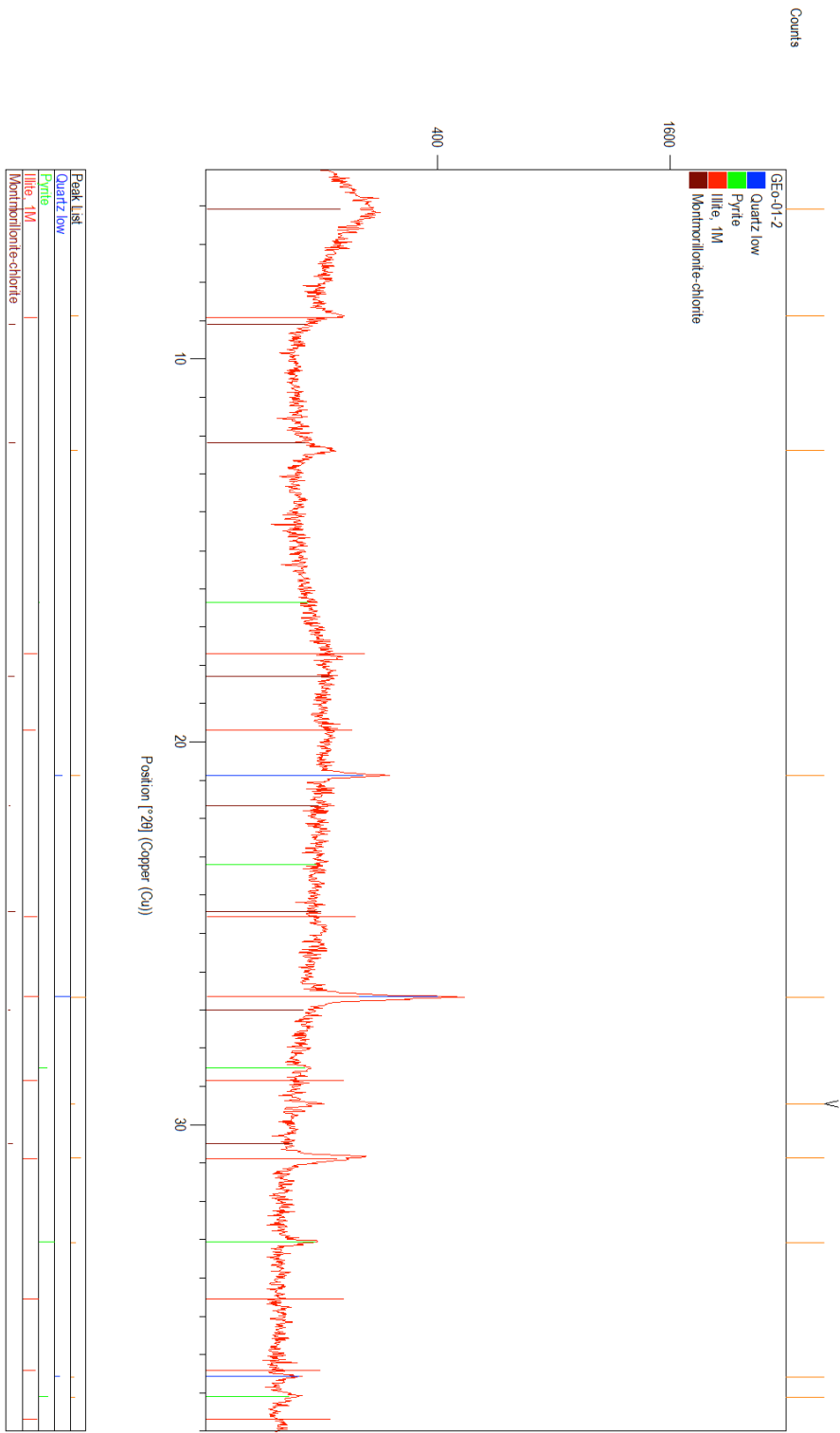
Figure 12: XRD pattern of sample GEo-01-2 (Table 5) demonstrating that the suspended load mainly consists of quartz, clay minerals and pyrite.
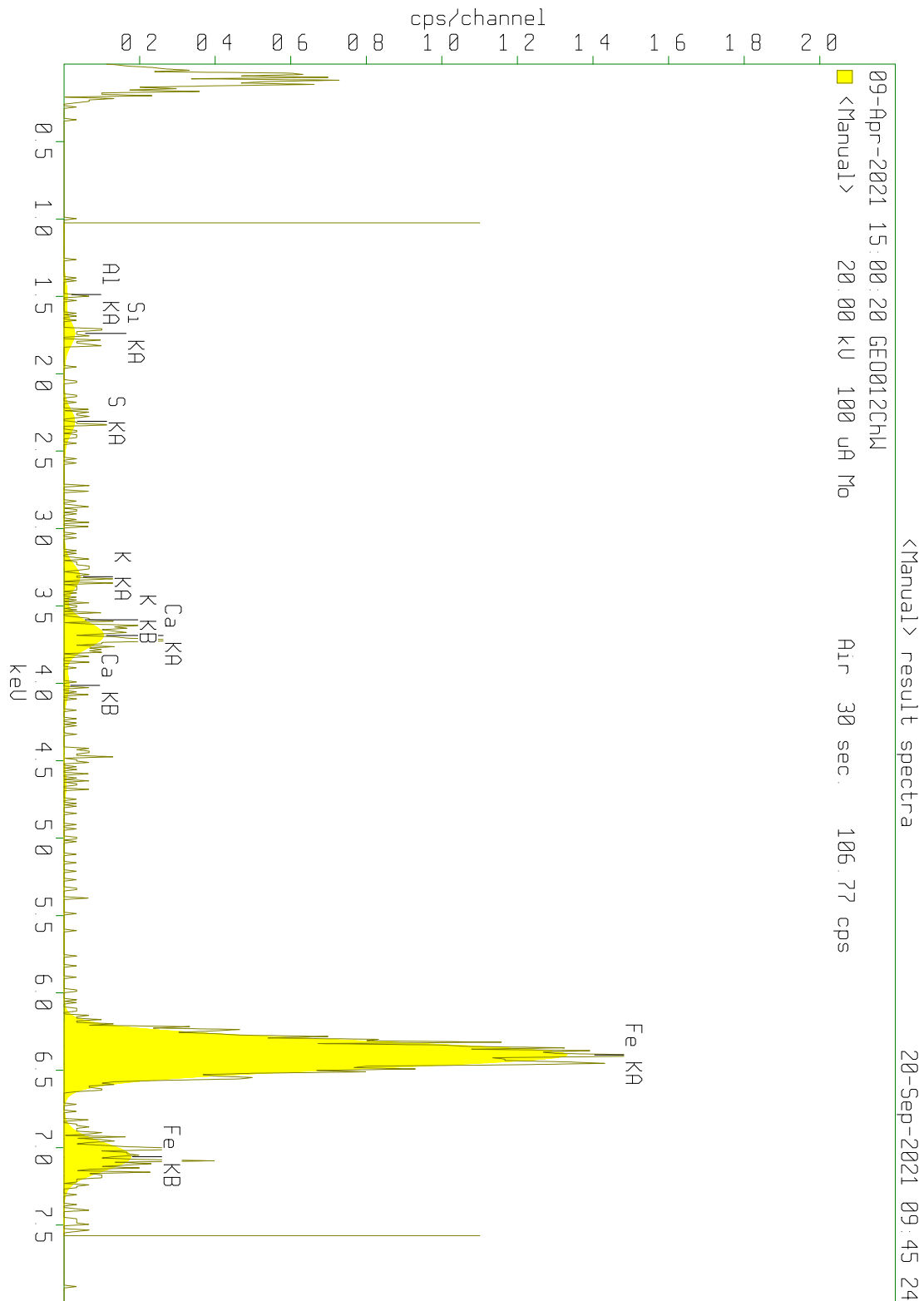
Figure 13: XRF spectrum of sample GEo-01-2 (Table 5) demonstrating that the suspended load mainly consists of Al, Si, Fe, S, K, and Ca consistent with the presence of quartz, clay minerals, and iron-bearing phases (Figure 11).
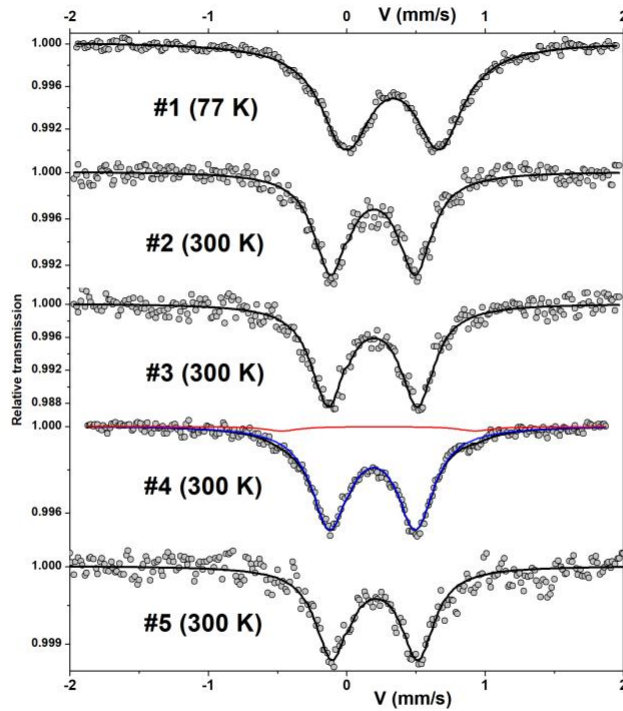
Figure 14: Recorded (open circles) and fitted (solid lines) Mössbauer spectra for the five suspended load samples (Figure 10). Note that the adsorption bands for sample GEo-01-1 (#1) occur at different velocities (V) than the other samples. This relates to the difference in the Fe oxidation state inherited from the presence of Fe^{3+} oxy-hydroxides whereas pyrite is the dominating Fe phase in all the other samples (Tables 5, 6).

Table 6: Mössbauer parameters

Sample	Temp (K)	I.S (mm/s)	F.H.M.W (mm/s)	Q.S./2ε (mm/s)	Area (%)	Identification
Geo-01-1 (#1)	77K	0.45	0.21	0.67	100%	Fe^{3+} oxy-hydroxides
Geo-01-2 (#2)	300K	0.31	0.29	0.6	100%	Pyrite
Geo-01-3 (#3)	300K	0.31	0.29	0.63	100%	Pyrite
Geo-01-4 (#4)	300K	0.31	0.32	0.61	96%	Pyrite
	300K	0.35	0.28	1.38	4%	Fe^{3+} oxy-hydroxides
Geo-01-5 (#5)	300K	0.32	0.29	0.61	100%	Pyrite

I.S. = Isomer shift value relative to that of the α-Fe at 300 K. (mm·s⁻¹)

F.W.H.M = Full width of line at half of its maximum intensity. (mm·s⁻¹)
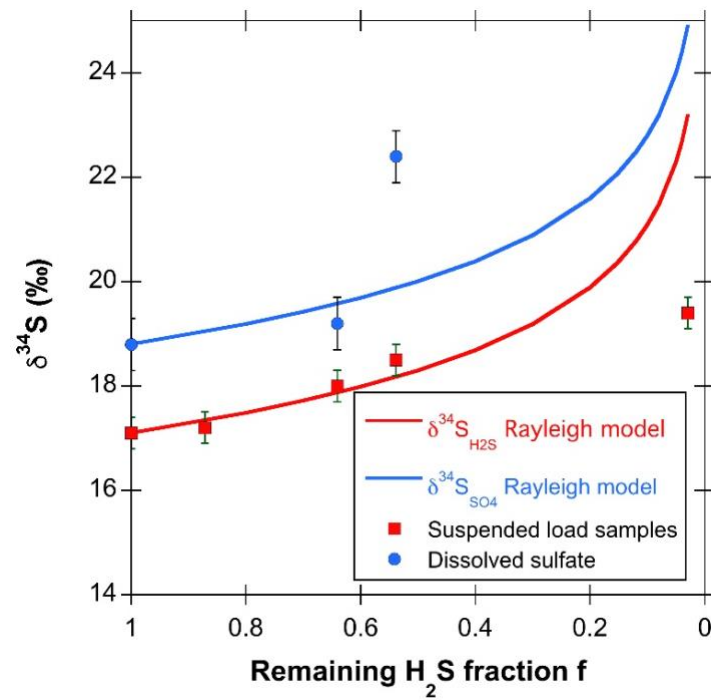
Q.S./2ε = Quadrupolar splitting

Figure 15: Rayleigh fractionation model describing the evolution of $\delta^{34}S$ values of the suspended load as well as sulphate (SO_4) dissolved in the thermal water as function of the H_2S concentration remaining with respect to the sample with the highest total sulphur concentration (GEo-01-5, Table 5). The thermal water ($\delta^{34}S_{SO4}$=22.4‰) and suspended load sample ($\delta^{34}S_{H2S}$ = 19.4‰) that do not follow the Rayleigh models were collected after the production of 0.2 and 0.04 well volumes and thus refer to the uppermost part of the GEo-01 well.

2.3.2. Microbial analyses

The concentration of microbes in the thermal water was greatest for the sample taken after producing for 0.44 well volumes (Figure 11b), which was also the sample showing the highest suspended load concentration. The sequencing data further demonstrates that the microbial community changed with production time (Figure 16). For the four samples taken during the production of the first well volume (Geo-01-1, Geo-01-2, Geo-01-3, Geo-01-4), Methanobacteria formed an important microbial class while it only appeared in trace amounts in the sample collected after 3.9 well volumes. In addition, the following Fe-oxidizing and Fe-reducing, as well as S-oxidizing and S-reducing bacterial genera were identified in these four samples:

Fe-oxidizer

Sideroxydans

Ferribacterium

Fe-reducer

Rhodoferax

S-oxidizer

Sulfuriferula

Paracoccus

32

| S-reducer | *Desulfotomaculum* | *Desulfurivibrio* | *Syntrophus* |

With the exception of *Paracoccus*, none of these bacteria could be identified in the sample collected after producing 3.9 well volumes.
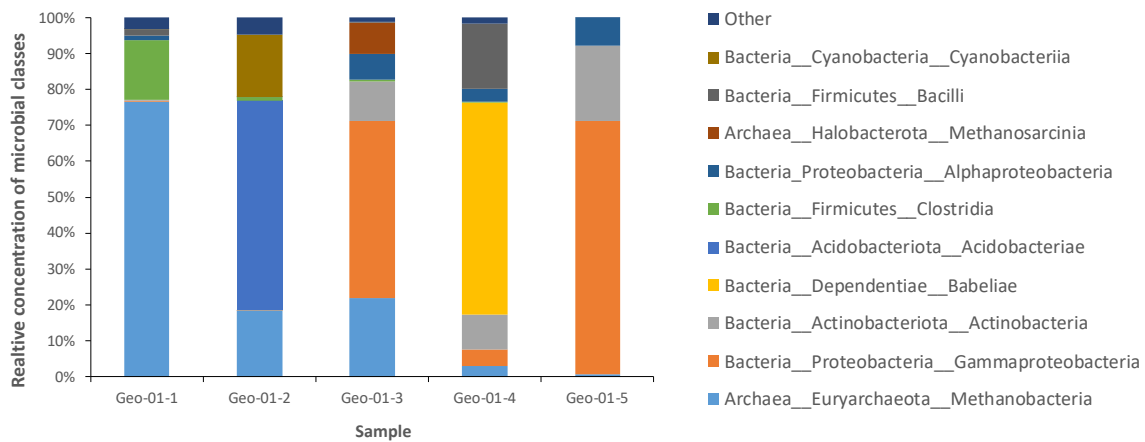

Figure 16: Relative concentrations of the 10 most abundant microbial classes in the thermal water samples produced from GEo-01 (Table 5). The three hierarchical levels in the legend refer to domain, phylum, and class.

2.4.   Discussion - Biogeochemical processes occurring in the GEo-01 well

The strong variations of the concentration and isotopic composition of oxidized and reduced sulfur species (Table 5, Figure 11a) demonstrate that the sulfur system is highly reactive in the GEo-1 well. Based on the identification of pyrite in the suspended load samples, the generally increasing total sulfur concentration with increasing production time, the short-term maximum of oxidized sulfur species, and the minimum Ca and HCO_3 concentrations observed in the water samples taken after producing for 2 minutes only, the following processes are interpreted to have taken place in the well:

- Corrosion of the steel casing and precipitation of pyrite
- Reduction of sulfate to sulfide
- Oxidation of sulfide to sulfate
- Precipitation of calcite

The identification of both sulfur and iron metabolizing microbes in the produced thermal water confirms the strong reactivity of the sulfur system and demonstrates that it was mediated by microbial activity.

Based on the processes listed above, a conceptual model of iron-corrosion and sulfur reactivity was developed (Figure 17). The model assumes that the thermal water in the main reservoir is characterized by initial concentrations of sulfide and sulfate similar to those measured in the thermal water sample collected after the production of 3.9 well volumes (i.e. sample GEo-01-5, Table 5). Upon production, the thermal water enters the GEo-01 well and coupled biogeochemical reactions with the steel casing are initiated. The sequence of processes is described in the following subsections.
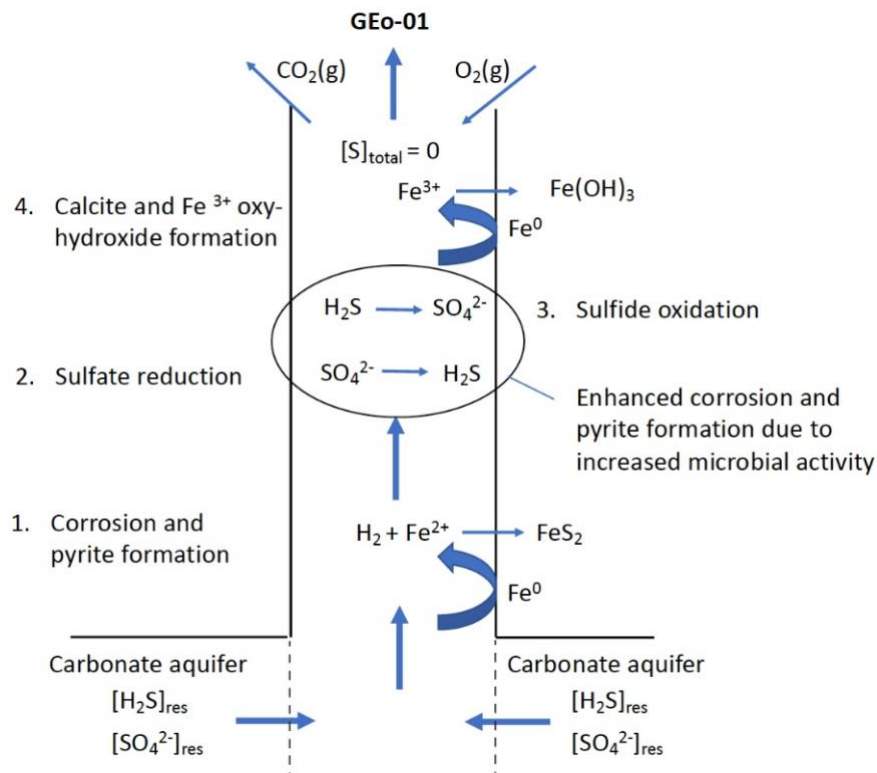

Figure 17: Conceptual model showing that four main biogeochemical reactions take place in the GEo-01 well. The ellipsoid highlights that enhanced corrosion and pyrite (FeS_2) formation occurs towards the top of the well, likely caused by the ingress of O_2 promoting microbially mediated iron corrosion, sulphide oxidation, and sulphate reduction.

1. <u>Corrosion of the casing and precipitation of pyrite</u>

Owing to the corrosive nature of hydrogen sulphide (Ma et al., 2000), the high total H_2S content of the thermal water (Table 5) leads to corrosion of the steel casing when the thermal water enters the GEo-01 well upon production:

$$Fe^0 + 2\,H^+ = Fe^{2+} + H_2 \tag{2}$$

Based on the identification of iron oxidizers, corrosion may be mediated by microbes. Hydrogen (H_2) produced by the corrosion reaction serves as an energy source for the identified methane-producing microbes via the following microbially-mediated reaction:

$$CO_2 + 4\,H_2 = CH_4 + 2\,H_2O \tag{3}$$

The high abundance of methane-producing microbes in the produced thermal water (Figure 16) is thus caused by the production of hydrogen, strongly confirming that anaerobic corrosion (Eq. (2)) is currently occurring in the GEo-01 well. Since the solubility of pyrite is low under reducing conditions, the Fe^{2+} cations generated by corrosion of the casing immediately precipitate as pyrite (FeS_2):

$$Fe^{2+} + 1.75\,HS^- + 0.25\,SO_4^{2-} + 0.25\,H+ = FeS_2 + H_2O \tag{4}$$
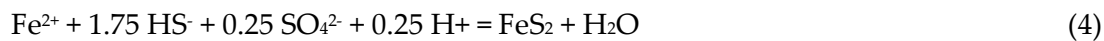
The coupled iron corrosion and pyrite precipitation likely occurs at the surface of the steel casing. The overall reaction can be written as:

$$Fe^0 + 2.25\,H^+ + 1.75\,HS^- + 0.25\,SO_4^{2-} = FeS_2 + H_2O + H_2 \tag{5}$$
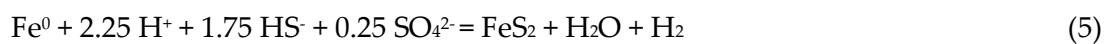
2. Reduction of sulphate to sulphide

Due to the precipitation of pyrite, the hydrogen sulphide and thus the total sulphur concentration decrease during upflow of the thermal water in the well. To maintain reducing conditions, the precipitation of sulphide as pyrite is compensated by the reduction of sulphate to sulphide in the thermal water.

Based on the identification of sulphate reducers, sulphate reduction is mediated by microbes. Microbial sulphate reduction and/or pyrite formation is likely the reason why the suspended load and thermal water samples collected after producing more than 0.2 well volumes nicely follow a Rayleigh fractionation model (Figure 15).

The sequence of iron corrosion, pyrite formation and sulphate reduction is consistent with results from geochemical modelling using PHREEQC (Figure 18). The model assumes chemical equilibrium and that pyrite formation occurs instantaneously when the thermal water becomes supersaturated with respect to pyrite. Figure 18 demonstrates that the model is able to capture the evolution of the total H_2S concentration as a function of the iron corrosion progress occurring during upflow along the production well. In contrast, the model first over- and then underestimates the concentration of oxidized sulphur in the thermal water. The overestimation occurring in the lower part of the well (i.e. at low corrosion progress) is because the speciation calculations do not take into account that sulphate reduction is microbially mediated, which can lead to a redox disequilibrium in the thermal water. Likewise, the model underestimates the oxidized sulphur concentration because it does not take into account the oxidation of sulphide to sulphate likely occurring in the upper part of the well (i.e. at a high corrosion progress, see below).
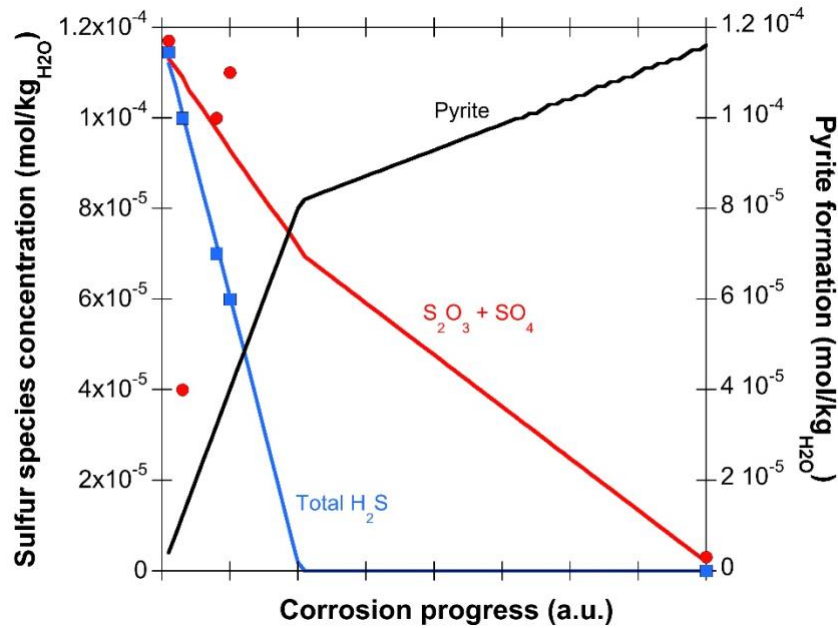
Figure 18: Results from geochemical modelling simulating the oxidation of metallic iron (i.e. the steel casing) occurring during upflow of the thermal water along the GEo-01 well, the subsequent precipitation of pyrite and the consequences for the sulphur species concentrations (solid lines). Thus, a low corrosion progress corresponds to deeper parts of the well, while higher values refer to locations closer to the surface. The filled symbols refer to the measured concentrations of total sulphur species. The corresponding iron corrosion progress was calibrated by the simulated evolution of the total H_2S concentration curve.

3. <u>Oxidation of sulphide to sulphate</u>

During downtime of the well, oxygen from the atmosphere starts to diffuse into the well. This leads to the oxidation of sulphide dissolved in the thermal water as manifested by the temporal maximum of the oxidized sulphur species concentrations observed after having produced for 0.2–0.5 well volumes (Figure 11a). Based on the presence of sulphide oxidizers, also this process is mediated and promoted by microbial activity. The occurrence of a second process in addition to sulphate reduction is further supported by the fact that the samples taken after producing for less than 0.2 well volumes do not follow the same Rayleigh fraction model as those originating from a deeper portion along the GEo-01 well (Figure 15).

Based on the coincidence of the temporal maximum of oxidized sulphur species and the maximum of both the dissolved load and the microbial concentration in the sample taken after producing for 0.4 well volumes (Figure 11), the ingress of oxygen from the atmosphere likely leads to an acceleration of the corrosion rate and thus the precipitation of pyrite. This is consistent with the study of Westphal et al. (2016) showing that sulphur scale formation was enhanced during a downtime period of the aquifer thermal energy storage facility in Neubrandenburg, Germany. In their study, enhanced scaling formation was further

attributed to the interaction of sulphide oxidizers and sulphate reducers leading to a strong increase of iron corrosion rates.

For the GEo-1 well, the entire suite of reactions involving sulphur species was so efficient that the top of the well (i.e. the sample collected after producing for 0.04 well volumes only) was entirely sulphur free after a downtime period of 3 months (Table 5, Figure 11a). The absence of sulphur, in turn, led to an excess of oxygen and thus to aerobic corrosion at the top of the well, as manifested by the presence of nanocrystalline Fe^{3+}-bearing oxy-hydroxides (e.g. $Fe(OH)_3$) in the corresponding suspended load sample.
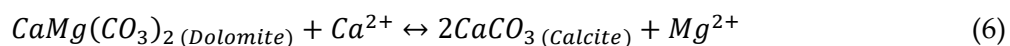
4. <u>Precipitation of calcite</u>

Since the CO_2 partial pressure of the produced thermal water strongly exceeds the one of the atmosphere ($10^{-2.3}$ vs. $10^{-3.5}$ bar), CO_2 degasses from the well during downtime. As a consequence, the pH increases and calcite starts to precipitate as manifested by the drop in Ca and HCO_3 observed in the samples collected after producing for 0.04 well volumes (Table 5). Based on the absence of significant amounts of calcite in the corresponding suspended load sample and the high degree of calcite supersaturation, however, calcite formation appears to be less efficient than the formation of pyrite during downtime of the GEo-01 well.

3. Implications for a potential HT-ATES system in the Geneva Basin

3.1. Mineral reactions inside the reservoir

During HT-ATES in a carbonate reservoir, the dissolution of dolomite is observed. Concurrently, calcite precipitation takes place, removing Ca from solution:

$$CaMg(CO_3)_{2\ (Dolomite)} + Ca^{2+} \leftrightarrow 2CaCO_{3\ (Calcite)} + Mg^{2+} \qquad (6)$$

Equation 6 shows that per mol of dolomite dissolved, two moles of calcite are precipitated. The molar volume of dolomite is 64.3 cm³/mol while that of calcite is slightly more than half of it (36.9 cm³/mol). Therefore, the dissolution and re-precipitation of the carbonate minerals according to equation 6 would result in a small decrease in porosity. However, our experimental observations suggest that the ratio of dissolved dolomite to precipitated calcite is smaller than 1:2. Firstly, we see an increase in the concentration of HCO_3^- at all temperatures, suggesting that not all carbonate ions released from the dissolution of dolomite are incorporated into newly formed calcite. Secondly, the increase in magnesium concentration and the decrease in calcium do not correspond. At 20 °C, two times more Mg is released into solution than Ca removed from solution. At higher temperatures the difference becomes

smaller but still around 1.5 times more Mg than Ca is released. One possible explanation is the non-stoichiometric dissolution of dolomite. Pioneering work by Busenberg & Plummer (1982) showed that the $CaCO_3$ component of dolomite reacted faster, resulting in a greater Ca/Mg ratio released into solution than that of the bulk solid. A more recent study on the dissolution of dolomite in the presence of organic molecules showed a reversed ratio, indicating a preferential Mg release (Veetil et al., 2017). In our experiments, we have a TOC concentration of 10 to 40 mg/L. While we do not know which kind of organic molecules are present, they might be the reason for incongruent dolomite dissolution. Another possibility is that the dissolution of dolomite is congruent but calcite precipitation is inhibited. Both the presence of organic acids as well as magnesium, sulphate and or phosphate have been shown to impede calcite formation (Griffioen & Appelo, 1993). As the APW contains around 0.6 mmol/L of magnesium, 0.3 mmol/L sulphate and several tens of mg/L of organic carbon, it is possible that one of these ions acts as an inhibitor.

These considerations only apply to our batch experiments and not an actual HT-ATES system where fluid is moving through the reservoir. In order to get a better understanding on how fluid flow affects the mineral reactions in the reservoir, a 3D THC model analogous to the one for Forsthaus (van den Heuvel et al., 2021) should be set up to better estimate (a) the amounts of minerals reacting and the spatially resolved effect on porosity as well as (b) mineral scaling (dissolution of carbonates in the reservoir will lead to scaling upon heating of said water in the heat exchanger). Such a model additionally allows to change parameters (e.g. temperature or pH) to assess how this could affect mineral reactions in the reservoir.

3.2. Corrosion and scaling in the GEo-01 well during shut-in

Based on the high reactivity of the sulphur system and the saturation with respect to calcite and dolomite discussed above, the following risks are associated with the use of the thermal water produced from GEo-01 for HT-ATES:

1. Corrosion of technical installations such as pumps, casings, and heat exchangers may occur due to high sulphide concentrations. This could lead to material failure and operational problems.
2. Owing to their retrograde solubility (i.e. decreasing solubility with increasing temperature), carbonates such as calcite will likely precipitate when the waters are heated to 90 °C during storage cycles. This could impede flow and heat exchange in the surface installations.

Our data suggest that corrosion is promoted during downtime periods. As a consequence, these should be minimized as much as possible. Technical problems related to corrosion could be further minimized by using stainless steel installations such as shown at the HT-ATES facility in Neubrandenburg, Germany (Lerm et al., 2013, Würdemann et al., 2014).

The precipitation of calcite upon heating is highly sensitive to complicated nucleation processes and may be kinetically limited (van den Heuvel et al., 2021). Thus, the precipitation rate depends on the geometry and materials of heat exchangers and it is challenging to predict the scaling rate under realistic field-site conditions. As a consequence, the scaling rate relevant for a particular HT-ATES system has to be evaluated on-site by performing field-scale heat storage tests.

Nevertheless, to obtain a rough estimate of the calcite scaling potential for the Geneva Basin we have calculated the maximum amount of calcite that could potentially precipitate per day in a hypothetical heat exchanger when heating the GEo-1 groundwater to 90 °C at a production rate of 50 L/s. For comparison, we have repeated this calculation for two GEo-02 groundwaters (Figure 19). This estimate is based on geochemical modelling using PHREEQC and represents a worst-case scenario where the saturation index of calcite is fixed to zero during heating. With 38 dm^3/day, the calcite scaling potential is greatest for the sample collected from GEo-01. This is because, compared to GEo-02, the water originates from a shallower depth where the temperature difference to 90 °C is greater (Table 6). Figure 7 further demonstrates that the temperature dependence of the calcite solubility is nearly linear and that the slope of the dependence varies with the water composition (e.g., pH, p_{CO_2}).

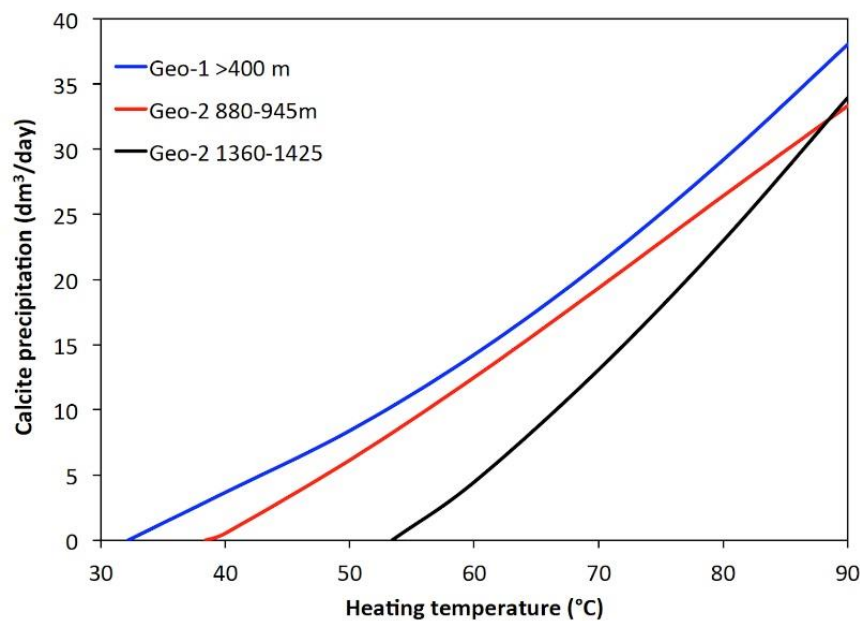*Figure 19. Maximum calcite volumes per day predicted to precipitate when groundwaters originating from GEo-1 and GEo-2 (Table 3) are produced at 50 L/s and heated to temperatures up to 90 °C.*

Table 7: Chemical composition of groundwater samples produced or pumped from GEO-1 and GEO-2

Well	Unit	GEO-01	GEO-02	GEO-02
Sampling date		09.60.2020	14.07.2020	14.07.2020
Sampling depth	m	>400 m	880-945	1360-1425
Sampling temperature	°C	32.2	21	20
In-situ reservoir temperature	°C	32.2	38.4	53.4
pH		7.7	8.41	8.22
Oxygen concentration	mg/L	0.1	5.7	1.7
Redox potential	mV	-281	384	395
Sodium (Na^+)	mg/L	32.7	152	52.5
Potassium (K^+)	mg/L	2.4	6.92	5.35
Calcium (Ca^{2+})	mg/L	28.1	16.0	35
Magnesium (Mg^{2+})	mg/L	14.2	8.0	14.2
Ammonium (NH_4^+)	mg/L	0.18	0.6	0.2
Bicarbonate (HCO_3^-)	mg/L	208	325	179
Chloride (Cl^-)	mg/L	9.9	31.2	15
Sulfate (SO_4^{2-})	mg/L	10.7	5.1	32.8
Nitrate (NO_3^-)	mg/L	< 0.2	< 0.1	< 0.1
Sulfide total (HS^-, S^{2-})	mg/L	3.9	not meas.	not meas.
Iron (Fe^{2+})	mg/L	< 0.02	< 0.01	< 0.01
Water type (simplified)		$Ca-HCO_3$	$Ca-HCO_3$	$Na-HCO_3$
Saturation index calcite		0.15	0.57	0.45
Saturation index dolomite		-005	1.14	1.85
Log(p_{CO2}) at reservoir T		-2.37	-2.00	-1.85

References

Beckingham, L. E., Mitnick, E. H., Steefel, C. I., Zhang, S., Voltolini, M., Swift, A. M., Yang, L., Cole, D. R., Sheets, J. M., Ajo-Franklin, J. B., DePaolo, D. J., Mito, S., & Xue, Z. (2016). Evaluation of mineral reactive surface area estimates for prediction of reactivity of a multi-mineral sediment. Geochimica et Cosmochimica Acta, 188, 310–329.

Busenberg, E., & Plummer, N. (1982). The kinetics of dissolution of dolomite in CO_2-H_2O systems at 1.5 to 65 °C and 0 to 1 atm p_{CO2}. American Journal of Science, 282(1), 45-78.

Carroll, D. (1959) Ion exchange in clays and other minerals. Geological Society of America Bulletin 70, 749-779.

Chermak, J.A. and Rimstidt, J.D. (1990) The hydrothermal transformation rate of kaolinite to muscovite/illite. Geochimica et Cosmochimica Acta 54, 2979-2990.

Deelman, J. C. (2003). Low-temperature formation of dolomite and magnesite. Eindhoven: Compact disc publications.

Eric Giffaut, Mireia Grivé, Philippe Blanc, Philippe Vieillard, Elisenda Colàs, Hélène Gailhanou, Stéphane Gaboreau, Nicolas Marty, Benoit Madé, Lara Duro. Andra thermodynamic database for performance assessment: ThermoChimie. Applied Geochemistry, 49 (2014) 225-236.

Gregg, J. M., Bish, D. L., Kaczmarek, S. E., & Machel, H. G. (2015). Mineralogy, nucleation and growth of dolomite in the laboratory and sedimentary environment: A review. Sedimentology, 62(6), 1749–1769.

Griffioen, J. and Appelo, C.A.J. (1993) Nature and extent of carbonate precipitation during aquifer thermal energy storage. Applied Geochemistry 8, 161-176.

Guglielmetti L., P. A.-E., Birdsell D., De Oliveira Filho F., Diamond L., Driesner T., Eruteya O., Hollmuller P., Makhloufi Y., Marti U., Martin F., Meier P., Meyer M., Mindel J., Moscariello A., Nawratil de Bono C., Quiquerez L., Saar M., Sohrabi R., Valley B., van den Heuvel D. and Wanner C. (2020) HEATSTORE SWITZERLAND: New Opportunities of Geothermal District Heating Network Sustainable Growth by High Temperature Aquifer Thermal Energy Storage Development. Proceedings World Geothermal Congress 2020 Reykjavik, Iceland, April 26-May 1, 2020.

Gunnlaugsson, E., & Einarsson, A. (1989). Magnesium-silicate scaling in mixture of geothermal water and deaerated fresh water in a district heating system. Geothermics, 18(1-2), 113-120.

Güntert N. (2020) Analyse und Modellierung des Grundwassers für geothermische Energiespeicherung im Genfer Becken. Unpublished B.Sc. Thesis University of Bern.

Harder, H. (1972). The role of magnesium in the formation of smectite minerals. Chemical Geology, 10(1), 31–39.

Hauksson, T., Thorhallsson, S., Gunnlaugsson, E., & Albertsson, A. (1995). Control of Magnesium Silicate Scaling in District Heating Systems. World Geothermal Congress, 2487–2490.

Kaczmarek, S. E., & Thornton, B. P. (2017). The effect of temperature on stoichiometry, cation ordering, and reaction rate in high-temperature dolomitisation experiments. Chemical Geology, 468(June), 32–41.

Lerm S., Westphal A., Miethling-Graff R., Alawi M., Seibt A., Wolfgramm M. and Würdemann H. (2013) Thermal effects on microbial composition and microbiologically induced corrosion and mineral precipitation affecting operation of a geothermal plant in a deep saline aquifer. Extremophiles 17, 311-327.

Ma H., Cheng X., Li G., Chen S., Quan Z., Zhao S. and Niu L. (2000) The influence of hydrogen sulfide on corrosion of iron under different conditions. Corrosion Science 42, 1669-1683.

Montes-Hernandez, German, Findling, N., & Renard, F. (2016). Dissolution-precipitation reactions controlling fast formation of dolomite under hydrothermal conditions. Applied Geochemistry, 73, 169–177.

Palandri, J. L., & Kharaka, Y. K. (2004). A compilation of rate parameters of water-mineral interaction kinetics for application to geochemical modeling. Geological Survey Menlo Park CA.

Parkhurst, D. L., & Appelo, C. A. J. (2013). Description of input and examples for PHREEQC version 3: a computer program for speciation, batch-reaction, one-dimensional transport, and inverse geochemical calculations (No. 6-A43). US Geological Survey.

Usdowski, E. (1989). Synthesis of dolomite and magnesite at 60° C in the system Ca 2+-Mg 2+-Co 3 2--C1 2 2--H 2 O. Naturwissenschaften, 76(8), 374-375.

van den Heuvel D., Alt-Epping P., Richards J., Wanner C. and Diamond L. (2021) Pre-study of the Forsthaus Geospeicher heat storage and utilisation project: Geological and geochemical aspects. Technical report by the Rock-Water Interaction Group, University of Bern.

Veetil, S. P., Mucci, A., & Arakaki, T. (2017). Dolomite dissolution in aqueous solutions in the presence of nucleotides and their structural components at 25 C and pCO2~ 1 atm. Chemical Geology, 465, 64-74.

Wersin, P., Mazurek, M., Waber, N., M der, U., Gimmi, T., Rufer, D. and De Haller, A. (2013) Rock and porewater characterisation on drillcores from the Schlattingen borehole, Nagra Arbeitsbericht NAB 12-54, Nagra, Wettingen, p. 343

Westphal A., Lerm S., Miethling-Graff R., Seibt A., Wolfgramm M. and Würdemann H. (2016) Effects of plant downtime on the microbial community composition in the highly saline brine of a geothermal plant in the North German Basin. Applied Microbiology and Biotechnology 100, 3277-3290.

Wiederhold J. G. (2015) Metal stable isotope signatures as tracers in environmental geochemistry. Environ. Sci. Technol. 49, 2606-2624.

Würdemann H., Westphal A., Lerm S., Kleyböcker A., Teitz S., Kasina M., Miethling-Graff R., Seibt A. and Wolfgramm M. (2014) Influence of Microbial Processes on the Operational Reliability in a Geothermal Heat Store – Results of Long-term Monitoring at a Full Scale Plant and First Studies in a Bypass System. Energy Procedia 59, 412-417.

Xu, J., Yan, C., Zhang, F., Konishi, H., Xu, H., & Teng, H. H. (2013). Testing the cation-hydration effect on the crystallisation of Ca–Mg–CO3 systems. Proceedings of the National Academy of Sciences, 110(44), 17750-17755.